J. Fluid Mech. (2021), *vol.* 918, A35, doi:10.1017/jfm.2021.354

Three-dimensional wake transition of a diamond-shaped cylinder

Hongyi Jiang†

School of Engineering, The University of Western Australia, 35 Stirling Highway, Perth, WA 6009, Australia

(Received 24 August 2020; revised 6 February 2021; accepted 18 April 2021)

Three-dimensional (3-D) wake transition for flow past a diamond cylinder is investigated numerically. Detailed 3-D direct numerical simulations (DNS) show that the wake is represented by mode A with global vortex dislocations for Reynolds numbers $Re = 121$–150, followed by a mode swapping between modes A and B for $Re = 160$–210 and increasingly disordered mode B for $Re \geq 220$. In the mode swapping regime, different characteristics of the dislocation and non-dislocation periods are revealed by decomposing flow properties (e.g. the root-mean-square lift coefficient) into the values corresponding to the dislocation and non-dislocation periods. Such decomposition helps to explain some major differences observed for the cases of a diamond and a circular cylinder. In addition to DNS, Floquet stability analyses are conducted to identify the 3-D wake instability modes of a diamond cylinder up to $Re = 300$. Phase-averaged base flow is used to eliminate the quantitative uncertainties induced by the aperiodic secondary vortex street of the base flow. Interestingly, a subharmonic instability mode is identified at $Re \geq 285$, whereas mode B is absent. The origin of the subharmonic mode is explained. The disagreement between the DNS and the Floquet analysis regarding the existence of mode B and the subharmonic mode is also explained. It is found that the natural 3-D flow involves complex interactions between the streamwise and spanwise vortices, as well as between the 3-D wake transition and the two-dimensional base-flow transition, which excite mode B and suppress the subharmonic mode.

Key words: wakes, vortex instability, vortex streets

1. Introduction

Steady incoming flow past a smooth and nominally two-dimensional (2-D) bluff body has been a classical problem in fluid mechanics. Commonly used bluff bodies include cylinders with circular and square cross-sectional shapes, for which the flow is governed by a single dimensionless parameter, i.e. the Reynolds number Re ($= UL/\nu$), defined based

† Email address for correspondence: hongyi.jiang@uwa.edu.au

on the incoming flow velocity (U), the length scale of the cylinder perpendicular to the incoming flow (L) and the kinematic viscosity of the fluid (ν). For a circular cylinder, the length scale is the diameter of the cylinder, commonly denoted D. For a square cylinder, the length scale depends on the flow incidence angle. For a square cylinder aligned with the four sides perpendicular and parallel to the incoming flow, which is commonly referred to as a square cylinder with zero flow incidence/attack angle (e.g. Tong, Luo & Khoo 2008; Sheard, Fitzgerald & Ryan 2009; Yoon, Yang & Choi 2010) or simply a square cylinder (e.g. Robichaux, Balachandar & Vanka 1999; Sohankar, Norberg & Davidson 1999; Blackburn & Lopez 2003), the length scale is the side length of the cylinder, commonly also denoted D. On the other hand, for a square cylinder aligned with all four sides 45 ° to the incoming flow, i.e. with an incidence angle $\alpha = 45^\circ$ and commonly referred to as a diamond cylinder, the length scale, commonly denoted h (e.g. Sheard *et al.* 2009; Yoon *et al.* 2010), is $\sqrt{2}$ times the side length of the cylinder. To be consistent with previous studies, the present study uses the terms 'square cylinder' and 'diamond cylinder' for the cases with $\alpha = 0^\circ$ and 45 °, respectively.

Three-dimensional (3-D) wake transitions for a circular and a square cylinder have been studied extensively in the literature through physical experiments, linear/nonlinear stability analyses and direct numerical simulations (DNS). With the increase in Re, a few wake transition regimes appear.

(i) At $Re \sim 190$ for a circular cylinder (Barkley & Henderson 1996; Williamson 1996) and $Re \sim 165$ for a square cylinder (Sheard *et al.* 2009; Choi, Jang & Yang 2012; Park & Yang 2016), the wake transitions from two- to three-dimensional through the mode A instability that originates in the primary vortex cores (Williamson 1996; Leweke & Williamson 1998; Thompson, Leweke & Williamson 2001). The mode A instability is subcritical in nature and contains a small hysteresis loop (Henderson & Barkley 1996; Henderson 1997; Akbar, Bouchet & Dušek 2011). The mode A streamwise vortices display an out-of-phase sequence (Williamson 1996) and a relatively large spanwise wavelength/period of $\sim 4D$ for a circular cylinder (Barkley & Henderson 1996) and $\sim 5D$ for a square cylinder (Choi *et al.* 2012; Park & Yang 2016). The ordered mode A structure is unstable over time and will evolve spontaneously into a more stable pattern with vortex dislocations (Williamson 1996). For $Re \sim 190$–230 for a circular cylinder (Williamson 1996) and $Re \sim 165$–185 for a square cylinder (Jiang, Cheng & An 2018*a*), the fully developed wake is represented by the pattern of mode A with vortex dislocations.

(ii) Over $Re \sim 230$–265 for a circular cylinder (Williamson 1996; Barkley, Tuckerman & Golubitsky 2000; Sheard, Thompson & Hourigan 2003) and $Re \sim 185$–210 for a square cylinder (Jiang *et al.* 2018*a*), the wake transitions gradually from the pattern of mode A with vortex dislocations to mode B. The mode B instability differs from the mode A instability in that it originates in the braid shear layer region (Williamson 1996; Leweke & Williamson 1998; Thompson *et al.* 2001) and is supercritical in nature (Henderson 1997). The mode B streamwise vortices display an in-phase sequence (Williamson 1996) and a relatively small spanwise wavelength/period of $\sim 0.8D$ for a circular cylinder (Barkley & Henderson 1996) and $\sim 1.1D$ for a square cylinder (Choi *et al.* 2012; Park & Yang 2016).

(iii) At $Re \sim 265$ for a circular cylinder (Williamson 1996; Barkley *et al.* 2000; Sheard *et al.* 2003) and $Re \sim 210$ for a square cylinder (Jiang *et al.* 2018*a*), the pattern of mode A with vortex dislocations disappears, beyond which the mode B structures become increasingly disordered, such that the wake becomes increasingly turbulent/chaotic. In particular, for a circular cylinder a critical condition is observed at $Re \sim 265$, where the mode B structures are particularly ordered, and a local peak or trough is observed for a number of flow properties, e.g. the base pressure coefficient and the Strouhal number (Williamson 1996).

An equally important case to the square cylinder is the diamond cylinder. Among the range of flow incidence angles, the square and diamond cylinders are the two special cases where the cross-sectional shape of the cylinder is symmetric about the wake centreline. In addition, at an *Re* corresponding to the wake transition from two- to three-dimensional, the 2-D wakes of both cylinders possess the Z_2 spatio-temporal symmetry, i.e. spatial reflection of the flow about the wake centreline after time evolution of every half-vortex shedding period (Blackburn & Sheard 2010; Yoon *et al.* 2010). Consistently, over the range of flow incidence angles, the cases of square and diamond cylinders correspond to local minima of *Re* for the onset of 3-D (specifically mode A) wake instability (Sheard *et al.* 2009; Yoon *et al.* 2010), i.e. the square and diamond cylinders are locally most unstable to the 3-D instability.

However, the 3-D wake transition process of a diamond cylinder is far less studied than that of a square or circular cylinder. The most well-understood aspect for a diamond cylinder is the onset of three-dimensionality, which is identified as the mode A instability at the critical *Re* (Re_{cr}) with the corresponding most unstable spanwise wavelength (λ_{cr}) of (Re_{cr}, λ_{cr}/h) = (116, 4.0) by Sheard *et al.* (2009) and (120, 4.2) by Yoon *et al.* (2010) through Floquet stability analysis, and $Re_{cr} = 127 \pm 2$ by Tong *et al.* (2008) through physical experiments. Beyond Re_{cr}, Floquet analysis has been routinely adopted in the literature in identifying additional instability modes in the cylinder wake. However, for a diamond cylinder the 2-D base flow becomes aperiodic at $Re \gtrsim 140$, which inhibits the application of Floquet analysis to higher *Re* values for the identification of additional instability modes other than mode A (Sheard *et al.* 2009). Alternatively, limited experimental and 3-D DNS cases (Tong *et al.* 2008; Yoon, Yang & Choi 2012; Jiang *et al.* 2018*b*) shed light on the wake structures beyond Re_{cr}. Tong *et al.* (2008) conducted physical experiments and identified a further wake transition from the mode A regime (with vortex dislocations) to the mode B regime at $Re = 190$. Yoon *et al.* (2012) performed 3-D DNS at a few *Re* values and observed ordered mode A structures at $Re = 150$, disordered mode A structures at $Re = 200$ and hardly identifiable structures at $Re = 250$. Jiang *et al.* (2018*b*) performed 3-D DNS and observed mode B structures at $Re \gtrsim 200$.

However, the wake structures reported by the above-mentioned studies do not agree well, and it is unclear whether the wake transition from mode A to mode B is a sudden or a gradual process.

In light of the earlier works, the present study aims at investigating in detail the wake transition process of a diamond cylinder based on 3-D DNS with a fine increment of *Re* of 10. A particular focus will be the gradual wake transition from mode A to mode B and the corresponding variations in the hydrodynamic forces.

The present study is also motivated by the aperiodicity of the base flow for a diamond cylinder and the consequent limitation to the Floquet stability analysis (Sheard *et al.* 2009). As will be shown in § 3.5, the aperiodicity of the base flow arises from the transition from the primary (Kármán) vortex street to the secondary vortex street within the relatively near wake (e.g. within 15*D* downstream of the cylinder for $Re \geq 200$). Therefore, interactions between the 3-D wake transition and the 2-D base-flow transition may be expected for the case of a diamond cylinder. Similar cases involving the base-flow transition relatively close to the cylinder include a thin rectangular cylinder (Saha 2007), a thin elliptical cylinder (Thompson *et al.* 2014), a triangular cylinder (Ng *et al.* 2016), etc. In contrast, for the cases of circular and square cylinders, the base flows over the 3-D wake transition regimes do not transition to the secondary vortex street within at least $50D$ downstream of the cylinder (e.g. Jiang & Cheng 2019), such that the 3-D wake transition and the 2-D base-flow transition are decoupled.

In the present study, the diamond cylinder serves as a representative case in investigating the interactions between the 3-D wake transition and the 2-D base-flow transition. In addition to the 3-D DNS, Floquet analysis is employed in providing a more thorough understanding of the interactions. The Floquet analysis will be conducted with caution, where the aperiodicity of the base flow will be tackled by particular measures.

2. Numerical model

2.1. *Numerical method*

DNS were conducted in this study in solving the flow around a diamond cylinder. The governing equations are the continuity and incompressible Navier–Stokes equations

$$\frac{\partial u_i}{\partial x_i} = 0, \tag{2.1}$$

$$\frac{\partial u_i}{\partial t} + u_j \frac{\partial u_i}{\partial x_j} = -\frac{1}{\rho}\frac{\partial p}{\partial x_i} + \nu \frac{\partial^2 u_i}{\partial x_j \partial x_j}, \tag{2.2}$$

where $(x_1, x_2, x_3) = (x, y, z)$ are the Cartesian coordinates, u_i is the velocity component in the direction x_i, t is time, ρ is fluid density, p is pressure and ν is kinematic viscosity. The numerical simulations were performed with the open-source code OpenFOAM (www.openfoam.org). The finite volume method (FVM) and the PISO (pressure implicit with splitting of operators) algorithm (Issa 1986) were used for solving the equations. The convection, diffusion and time derivative terms were discretised, respectively, using a fourth-order cubic scheme, a second-order linear scheme and a blended scheme consisting of the second-order Crank–Nicolson scheme and a first-order Euler implicit scheme. The same numerical approach was used in Jiang *et al.* (2016, 2018*a*) for the simulations of wake transition of a circular and a square cylinder.

2.2. *Computational domain and mesh*

A hexahedral computational domain, as sketched in figure 1(*a*), was used for the present DNS. As shown in figure 1(*a*), the centre of the diamond cylinder was placed at $(x, y) = (0, 0)$. The computational domain size was $-40 \leq x/h \leq 40$ in the streamwise direction, $-40 \leq y/h \leq 40$ in the transverse direction and $0 \leq z/h \leq 12$ in the spanwise direction. The spanwise domain size $L_z/h = 12$ was chosen based on Jiang, Cheng & An (2017*a*), who examined the effect of L_z on the numerical modelling of flow past a circular cylinder over the 3-D wake transition regimes, and demonstrated that an L_z of approximately three times the intrinsic wavelength of mode A is required to avoid inaccurate vortex patterns induced by the restriction of L_z. For the present case of a diamond cylinder, the spanwise wavelength of mode A at the onset of flow three-dimensionality is $4.00h$ (see § 2.4), such that $L_z/h = 12$ was used to accommodate three spanwise periods of mode A.

The boundary conditions for the velocity included a uniform velocity $(u_x, u_y, u_z) = (U, 0, 0)$ at the inlet, a Neumann condition (i.e. zero normal gradient) at the outlet and a no-slip condition on the cylinder surface. The boundary conditions for the pressure included a Neumann condition for the inlet and cylinder surface, and a reference

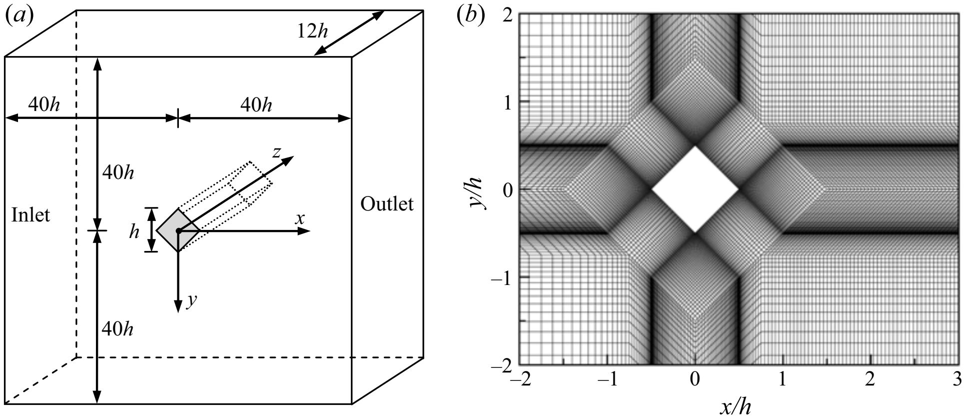

Figure 1. (*a*) Schematic model of the computational domain (not to scale), and (*b*) close-up view of the 2-D mesh near the cylinder.

of $p = 0$ at the outlet. Symmetry boundary conditions were applied at the top and bottom boundaries, while periodic boundary conditions were employed at the two lateral boundaries perpendicular to the cylinder span. The periodic boundary conditions allow for travelling waves in the spanwise direction (Jiang *et al.* 2017*a*) and follow the nature of the underlying instability modes which are spanwise periodic (e.g. Henderson 1997; Sheard *et al.* 2009). The internal flow followed an impulsive start.

The 2-D mesh in the x–y plane consisted of 92 828 cells. Figure 1(*b*) shows a close-up view of the 2-D mesh near the cylinder. The cylinder surface was discretised with 128 nodes. The height of the first layer of mesh next to the cylinder was $0.008h$, which resulted in the smallest cell size at the four corners of the cylinder being $0.008h \times 0.008h$. A relatively high resolution was used in the wake region by specifying the streamwise cell size at the wake centreline ($y = 0$) increasing linearly from $0.04h$ at $x/h = 1.5$ to $0.1h$ at $x/h = 20$. The 3-D mesh was constructed by replicating the 2-D mesh along the z-direction with a spanwise cell size $\Delta z = 0.1h$.

For each case, the time step size was fixed at $\Delta tU/h = 0.00186$, which corresponded to a Courant–Friedrichs–Lewy (CFL) limit of 0.5. The CFL number is defined as

$$\mathrm{CFL} = \frac{|u|\Delta t}{\Delta l}, \tag{2.3}$$

where $|u|$ is the magnitude of the velocity through a cell, and Δl is the cell size in the direction of the velocity.

2.3. *Mesh convergence*

Based on the reference mesh introduced in § 2.2, a mesh dependence study was performed at $Re = 250$ (the largest Re for the present DNS by OpenFOAM) with two variations.

(i) A mesh refined in the z-direction, where Δz was reduced from $0.1h$ to $0.05h$.
(ii) A mesh refined in the x–y plane, where the numbers of cells in both the x- and y-directions were 1.5 times those of the reference mesh, while the general topology of the mesh remained unchanged. In particular, the number of cells around the cylinder surface was increased by 1.5 times, while the height of the first layer of

Case	$\overline{C_D}$	C_L'	St	L_r/h
Reference	1.7213	0.4691	0.1800	1.3487
Refined in the z-direction	+0.34%	−0.11%	+0.46%	−0.76%
Refined in the x–y plane	+0.98%	+3.71%	+0.87%	−1.59%

Table 1. Mesh dependence check of some major flow properties for $Re = 250$. The results other than the reference case are shown by the relative differences with respect to those of the reference case.

mesh next to the cylinder was reduced by 1.5 times. For this case, the time step size was also reduced by 1.5 times so as to satisfy the CFL limit of 0.5.

Table 1 lists some major flow properties calculated with the three meshes. The drag and lift coefficients (C_D and C_L) and the Strouhal number (St) are defined as

$$C_D = \frac{F_D}{\frac{1}{2}\rho U^2 h L_z}, \tag{2.4}$$

$$C_L = \frac{F_L}{\frac{1}{2}\rho U^2 h L_z}, \tag{2.5}$$

$$St = \frac{f_L h}{U}, \tag{2.6}$$

where F_D and F_L are the drag and lift forces on the cylinder, respectively, and f_L is the frequency of the fluctuating lift force, which is determined as the peak frequency derived from the fast Fourier transform (FFT) of the time history of C_L. The time-averaged drag and lift coefficients are denoted $\overline{C_D}$ and $\overline{C_L}$, respectively. The root-mean-square lift coefficient is calculated as

$$C_L' = \sqrt{\frac{1}{N}\sum_{i=1}^{N}(C_{L,i} - \overline{C_L})^2}, \tag{2.7}$$

where N is the number of values in the time history. The wake recirculation length (L_r) is defined as the horizontal distance between the centre of the cylinder ($x/h = 0$) and the wake stagnation point, which is averaged over both time and the cylinder span. For each case listed in table 1, the time average was performed for at least 650 non-dimensional time units (defined as $t^* = tU/h$), after discarding an initial period of at least 350 non-dimensional time units.

As shown in table 1, the flow properties calculated with the two refined meshes are very close to those calculated with the reference mesh.

In addition, for the three cases listed in table 1, figure 2 shows the time-averaged and root-mean-square velocity profiles sampled at a few streamwise locations in the wake. The velocity profiles were also averaged over the cylinder span. The time-averaged streamwise and transverse velocities are denoted as $\overline{u_x}$ and $\overline{u_y}$, respectively, while the root-mean-square

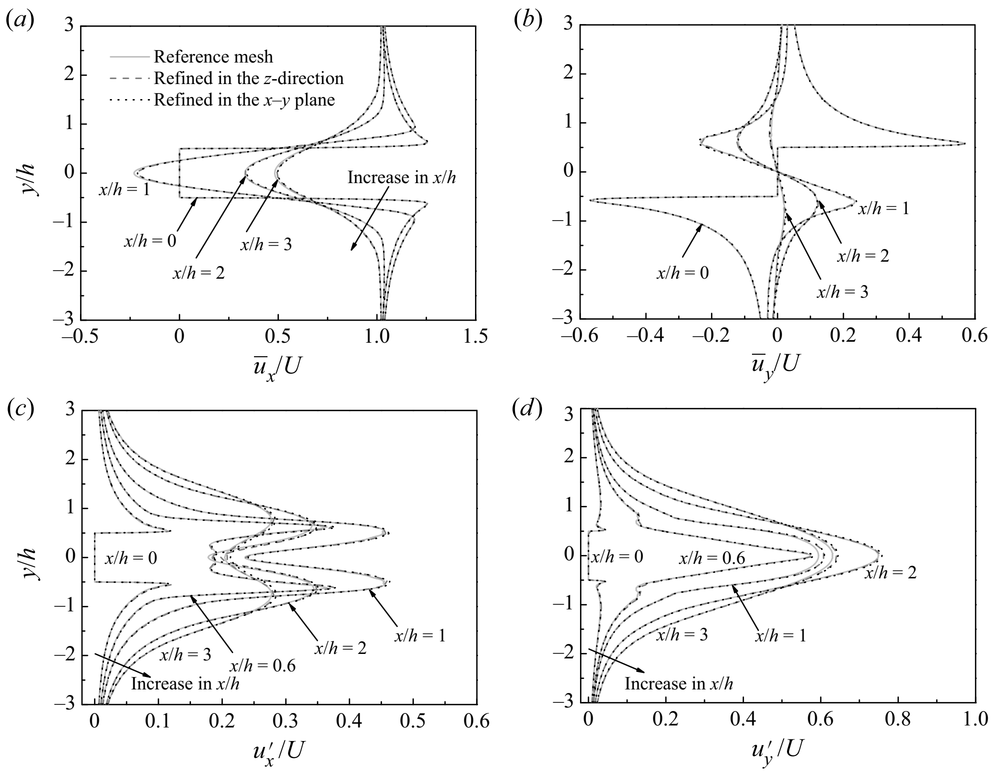

Figure 2. Mesh dependence check of the velocity profiles sampled at a few streamwise locations for $Re = 250$: (*a*) time-averaged streamwise velocity profiles, (*b*) time-averaged transverse velocity profiles, (*c*) root-mean-square streamwise velocity profiles and (*d*) root-mean-square transverse velocity profiles. The velocity profiles were also averaged over the cylinder span.

streamwise and transverse velocities are calculated as

$$u'_x = \sqrt{\frac{1}{N}\sum_{i=1}^{N}(u_{x,i} - \overline{u_x})^2}, \tag{2.8}$$

$$u'_y = \sqrt{\frac{1}{N}\sum_{i=1}^{N}(u_{y,i} - \overline{u_y})^2}. \tag{2.9}$$

As shown in figure 2, the velocity profiles calculated with the two variation cases agreed well with those calculated with the reference case, with the largest difference at any (x, y) location being smaller than $0.02U$. Based on the results shown in table 1 and figure 2, the reference mesh was considered adequate and was adopted for the present study.

2.4. *Onset of three-dimensionality*

For flow past a diamond cylinder, the flow transitions from two- to three-dimensional through the mode A wake instability (Tong *et al.* 2008; Sheard *et al.* 2009; Yoon *et al.* 2010). Floquet stability analysis has been a preferred method in determining the Re_{cr} and λ_{cr} values for this instability, e.g. (Re_{cr}, λ_{cr}/h) = (116, 4.0) by Sheard *et al.* (2009) and

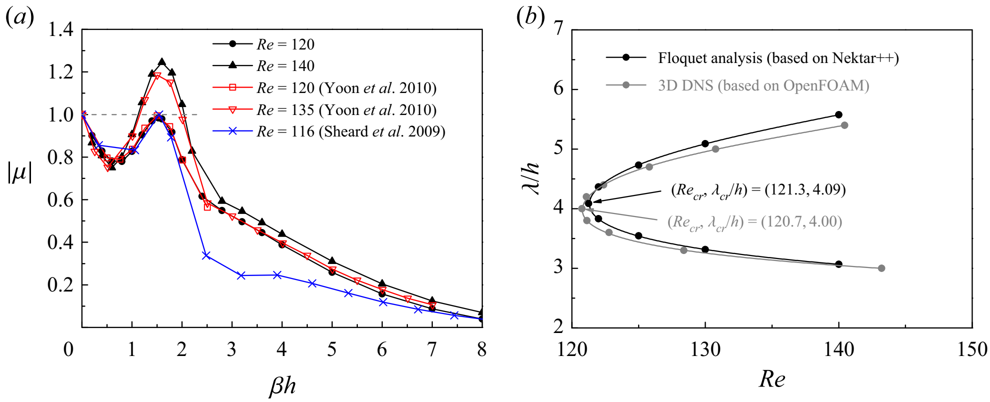

Figure 3. Floquet stability analysis results: (*a*) dependence of the dominant Floquet multiplier μ on the spanwise wavenumber β, and (*b*) the neutral instability curve of mode A.

(120, 4.2) by Yoon *et al.* (2010). In this section, Floquet analysis was used to confirm the (Re_{cr}, λ_{cr}/h) values and to map out the neutral instability curve for mode A. The present Floquet analysis followed the methodology presented in Barkley & Henderson (1996) and the numerical framework embedded in the open-source code Nektar++ (Cantwell *et al.* 2015) (since Floquet analysis is not readily available in the standard framework of OpenFOAM but has been well tested in Nektar++). The computational domain size used in Nektar++ for the Floquet analysis was the same as that introduced in § 2.2 for OpenFOAM. The macro-element mesh for Nektar++ used 32 macro-elements around the cylinder perimeter, $0.0388h \times 0.0388h$ for the smallest cell size at the four corners of the cylinder, and a relatively high wake resolution such that the streamwise cell size at the wake centreline increased linearly from $0.196h$ at $x/h = 1.5$ to $0.810h$ at $x/h = 40$. Overall, the macro-element mesh was approximately 4 to 5 times coarser in both the x- and y-directions than the mesh used in OpenFOAM. The macro-elements were then subdivided using fifth-order Lagrange polynomials ($N_p = 5$) on the Gauss–Lobatto–Legendre points for the quadrilateral expansions. Owing to the use of the high-order spectral/*hp* element method for Nektar++ (Karniadakis & Sherwin 2005), the overall mesh resolution for Nektar++ was finer than that for the FVM-based OpenFOAM.

Figure 3(*a*) shows the dependence of the dominant Floquet multiplier μ on the spanwise wavenumber β ($= 2\pi/\lambda$) for $Re = 120$ and 140, together with similar results predicted by Sheard *et al.* (2009) and Yoon *et al.* (2010). In figure 3(*a*), a single peak region of $|\mu| > 1.0$ is observed, where the μ values are real and positive, which suggests that this peak region corresponds to the mode A instability. Figure 3(*b*) shows the neutral instability curve of mode A. The (Re_{cr}, λ_{cr}/h) values for the present Floquet analysis are determined based on a linear interpolation of the peak $|\mu|$ values at $Re = 121$ and 122 to the neutral instability of $|\mu| = 1.0$. The results (Re_{cr}, λ_{cr}/h) = (121.3, 4.09) agree well with those reported by Sheard *et al.* (2009) and Yoon *et al.* (2010). In addition, a mesh convergence check was performed at (Re, λ/h) = (120, 4.107), where an increase in N_p from 5 to 7 resulted in a decrease in $|\mu|$ of 0.01 %, suggesting the use of $N_p = 5$ was adequate.

As shown in figure 3(*b*), the neutral instability curve for mode A was also calculated through 3-D DNS (based on OpenFOAM). For the DNS method, only a half of a spanwise period of the mode A structure was simulated (by using $L_z = \lambda/2$, $L_z/\Delta z = 10$ and symmetry boundary conditions at the two lateral boundaries to isolate a half of a spanwise period of mode A), such that the computational cost of this method was comparable to that of the Floquet analysis. More details on this method can be found in Jiang *et al.* (2017*b*). The present DNS method predicted $(Re_{cr}, \lambda_{cr}/h) = (120.7, 4.00)$, which agreed well with the results predicted by the Floquet analysis. In addition, a mesh convergence check at $L_z = \lambda/2 = 2h$ showed that by (i) doubling the mesh layers in the spanwise direction (to $L_z/\Delta z = 20$), (ii) doubling the cell numbers in both the x- and y-directions or (iii) doubling the domain size in the x–y plane (to $-80 \leq x/h \leq 80$ and $-80 \leq y/h \leq 80$), the variations in Re_{cr} were all within 1 %. In particular, variation case (i) predicted also $Re_{cr} = 120.7$. For the 3-D wake transition process investigated in § 3, the mesh resolution used in OpenFOAM was identical to that used in the variation case (i), such that $(Re_{cr}, \lambda_{cr}/h) = (120.7, 4.00)$ was directly applicable to the OpenFOAM cases examined in § 3.

3. Numerical results

3.1. *Three-dimensional wake transition*

In the present study, the 3-D wake transition beyond $Re_{cr} = 120.7$ was examined up to $Re = 250$. For each Re, the flow was deemed fully developed after a time integration of 1000 non-dimensional time units, which corresponded to ∼180 vortex shedding cycles. After that, at least another 1000 non-dimensional time units were used for the statistics and analysis of the fully developed flow. The wake transition process was identified through visualising the streamwise and spanwise vorticity (ω_x and ω_z) fields, where ω_x and ω_z are defined in a non-dimensional form as

$$\omega_x = \left(\frac{\partial u_z}{\partial y} - \frac{\partial u_y}{\partial z}\right)\frac{h}{U}, \tag{3.1}$$

$$\omega_z = \left(\frac{\partial u_y}{\partial x} - \frac{\partial u_x}{\partial y}\right)\frac{h}{U}. \tag{3.2}$$

Figure 4 illustrates the streamwise and spanwise vortex structures for Re in different wake transition regimes. In summary, with the increase in Re, the wake undergoes a transition sequence of 'mode A with global vortex dislocations ($Re = Re_{cr} - 150$) → mode swapping between modes A and B ($Re = 160$–210) → mode B ($Re \geq 220$)'.

Specifically, for $Re = Re_{cr} - 150$, the initial 3-D structure developed in the wake is a relatively ordered mode A structure (figure 4*b–d*). As shown in figure 4(*b–d*), the mode A structure originates and grows from the primary vortex cores, which is consistent with the origin of the mode A instability identified based on a circular cylinder (Williamson 1996; Leweke & Williamson 1998; Thompson *et al.* 2001). With the evolution over time, the relatively ordered mode A structure evolves into a pattern with vortex dislocations (figure 4*d–f*). The origin of the vortex dislocations shown in figure 4(*f*) can be traced back to a slight difference in strength in the three pairs of the mode A streamwise vortices shown in figure 4(*b–e*). Ever since the emergence of the three mode A streamwise vortex pairs at $t^* \sim 100$ (from figures 4*a* to 4*b*), pair 1 is always slightly stronger than the other two pairs (figure 4*b–e*). With the evolution in time, this stronger pair of mode A structure grows into a local vortex dislocation in figure 4(*e*). After that, the local vortex dislocation develops along the spanwise direction and engulfs the other two pairs of mode A structure, resulting in a pattern of global vortex dislocation for the saturated flow (figure 4*f*).

For the saturated flow, scattered mode A streamwise vortex pairs emerge intermittently. Depending on the Re value, the mode A streamwise vortex pairs developed in the wake (e.g. figure 4*d*,*g*,*j*) may evolve into one of the following two patterns:

(i) The mode A streamwise vortex pair evolves into a local vortex dislocation, e.g. pair 1 in figure 4(*d*,*e*) and pair 2 in figure 4(*g*,*h*).

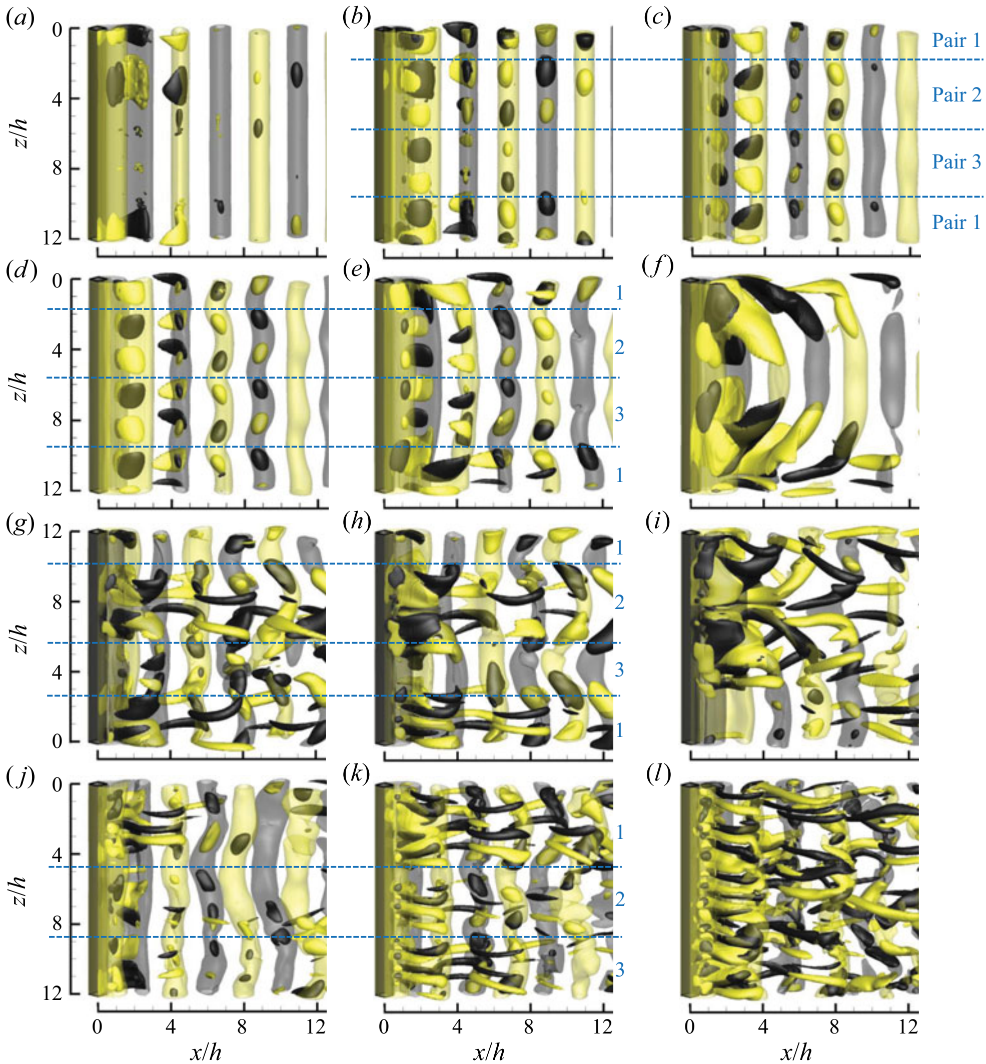

Figure 4. Instantaneous vorticity fields in the near wake of a diamond cylinder for (*a–f*) $Re = 125$ with $t^* = 80$, 120, 320, 400, 480 and 520, (*g–i*) $Re = 150$ with $t^* = 1605$, 1645 and 1675, (*j–k*) $Re = 190$ with $t^* = 1360$ and 1380 and (*l*) $Re = 240$ with $t^* = 2125$. The translucent iso-surfaces represent spanwise vortices with $\omega_z = \pm 1.0$, while the opaque iso-surfaces represent streamwise vortices with $\omega_x = \pm 0.02$ for panels (*a*,*b*), $\omega_x = \pm 0.3$ for panel (*c*), $\omega_x = \pm 0.5$ for panels (*d–f*), $\omega_x = \pm 0.8$ for panels (*g–i*), and $\omega_x = \pm 1.0$ for panels (*j–l*). Dark grey and light yellow denote positive and negative vorticity values, respectively. The flow is from left to right past the cylinder on the left.

(ii) The mode A streamwise vortex pair evolves into the mode B structure, e.g. pair 1 in figure 4(*g*) and pairs 2 and 3 in figure 4(*j*).

For $Re = Re_{cr} - 140$, only pattern (i) exists. Any particular mode A streamwise vortex pair that evolves through pattern (i) would engulf the unevolved mode A streamwise vortex pairs and lead to a pattern of global vortex dislocations (e.g. figure 4*d–f*). For $Re = 150$–210, both patterns exist. A special condition occurs at $Re = 150$, where although pattern (ii) exists occasionally, it is always accompanied by the co-existence of pattern (i) and would thus still evolve into global vortex dislocations (e.g. figure 4*g*–*i*). In summary, for $Re = Re_{cr} - 150$ the saturated flow is always represented by global vortex dislocations.

For $Re = 160$–210, global vortex dislocations appear intermittently in the saturated flow. Similar to $Re = 150$, any mode A streamwise vortex pair that evolves through pattern (i) would lead to global vortex dislocations, even when other mode A streamwise vortex pair(s) evolve through pattern (ii) at the same time (e.g. figure 4*g*–*i*). In contrast, global vortex dislocation is suppressed when all of the mode A streamwise vortex pairs evolve through pattern (ii) (e.g. figure 4*j*,*k*). This pattern (i)/(ii) of evolution results in an intermittent appearance of global vortex dislocations (i.e. mode swapping) for $Re = 160$–210.

The mode swapping over $Re = 160$–210 is quantified in figure 5. The shaded and clear blocks indicate dislocation and non-dislocation time periods, respectively, which are determined by visually examining the time evolution of the streamwise vorticity field (e.g. those shown in figure 4) with an interval of 10 non-dimensional time units. The global vortex dislocations are spotted easily as they appear over continuous time periods and normally occupy the entire domain (Jiang *et al.* 2016). Based on the time histories shown in figure 5, the probability of occurrence of dislocation is further quantified in figure 6. As shown in figure 6, the probability of occurrence of dislocation decreases monotonically with increasing *Re*. With the increase in *Re*, the mode B structures are more likely to be destabilised and in turn replace/stabilise the mode A streamwise vortex pairs through the pattern (ii) evolution, which results in a reducing likelihood of pattern (i), i.e. a reducing likelihood of dislocation. It is also noticed that the mode swapping shown in figure 5 is most frequent when the probability of occurrence of dislocation is close to 50%.

For $Re \geq 220$, pattern (i) no longer exists. Scattered mode A streamwise vortex pairs, which evolve through pattern (ii) only, are observed for <8% and <2% of the statistical time periods for $Re = 220$ and 250, respectively, which suggests that for $Re \geq 220$ the influence of mode A is minimal. The wake is dominated by disordered mode B structures, as illustrated in figure 4(*l*).

3.2. *Characteristics of the dislocation and non-dislocation periods*

Based on the separation of the dislocation and non-dislocation time periods in figure 5, the flow properties, such as the hydrodynamic forces on the cylinder, can also be decomposed into the values corresponding to the dislocation and non-dislocation time periods. Such an analysis has not been performed before in the literature, and is expected to shed new light on the different characteristics of the dislocation and non-dislocation periods.

Figure 7 shows the time histories of C_L for *Re* over the mode swapping regime, overlaid with shaded and clear regions representing dislocation and non-dislocation time periods, respectively. As shown in figure 7, the dislocation periods correspond to local reductions in the fluctuation amplitude of C_L, which include some extremely small fluctuation amplitudes over the time history. In particular, the long dislocation periods observed for $Re = 160$ consist of frequent local reductions in the fluctuation amplitude of C_L, except for the non-dislocation period at $t^* = 1280$–1420, where the fluctuation amplitude is sustained at a relatively large level.

The local reductions in the fluctuation amplitude of C_L for the dislocation periods originate from the local dislocations in the mode A streamwise vortices. As shown in figure 4(*e*,*f*,*h*,*i*), the local dislocations in the mode A streamwise vortices towards the upstream direction would induce an upstream movement of the corresponding fractions of the spanwise vortex rollers and eventually lead to inclined spanwise vortex rollers at the two sides of the local dislocation. The inclined spanwise vortex rollers shown

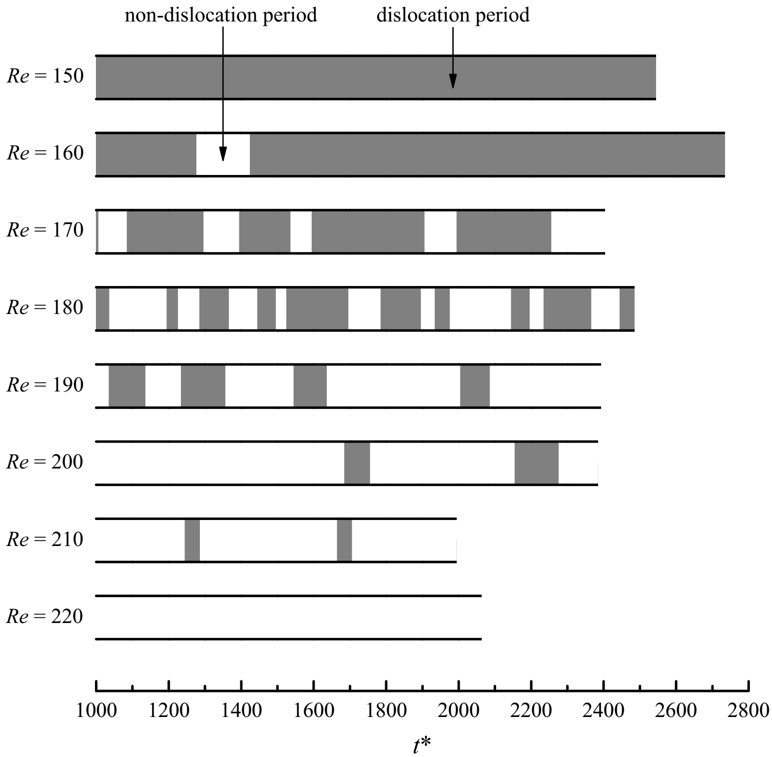

Figure 5. Quantification of the intermittent appearance of global vortex dislocations in the range of $Re = 150$–220. The shaded and clear blocks indicate dislocation and non-dislocation time periods, respectively.

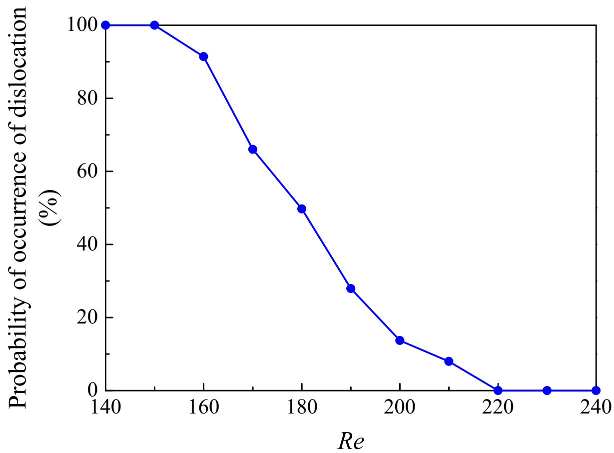

Figure 6. Probability of occurrence of vortex dislocation for *Re* over the mode swapping regime.

in figure 4(*f*,*i*) indicate phase differences in the primary vortex shedding at different spanwise locations up to at least 180° (the inclined spanwise vortex rollers may reach the streamwise location for the subsequent spanwise vortex roller), which partially cancels out the integrated lift coefficient. In contrast, the mixed mode A and B structures in the

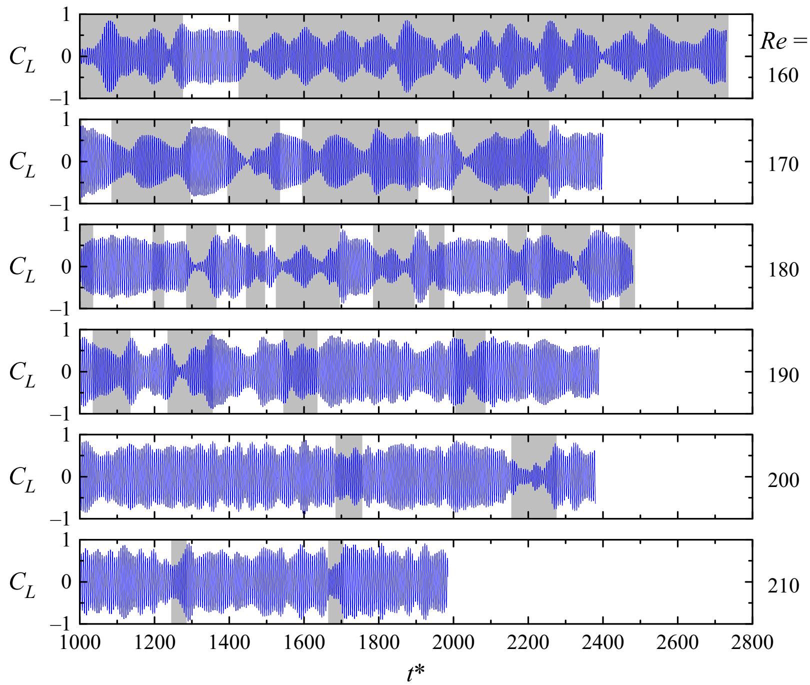

Figure 7. Time histories of the lift coefficient for $Re = 160$–210, overlaid with shaded and clear regions representing dislocation and non-dislocation time periods, respectively.

non-dislocation periods do not induce significant inclinations in the spanwise vortex rollers (e.g. figure 4*j*,*k*), such that the fluctuation amplitudes of C_L are relatively large.

Figure 8(*a*) shows the C_L'–Re relationship over the wake transition regimes. The C_L' values over the mode swapping regime are further decomposed into the ones corresponding to the dislocation and non-dislocation time periods. As expected, the C_L' values for the dislocation periods are consistently smaller than those for the non-dislocation periods. With the gradual decrease in the probability of occurrence of dislocation over $Re = 160$–210 (figure 6), the overall C_L' value moves gradually from the dislocation branch to the non-dislocation branch (figure 8*a*).

Figure 8(*b*) examines the degree of flow three-dimensionality in the wake, quantified by the time-averaged streamwise and transverse enstrophies (ε_x and ε_y) defined as

$$\varepsilon_x = \frac{1}{2}\int_V \omega_x^2 \, \mathrm{d}V, \tag{3.3}$$

$$\varepsilon_y = \frac{1}{2}\int_V \omega_y^2 \, \mathrm{d}V, \quad \text{where } \omega_y = \left(\frac{\partial u_x}{\partial z} - \frac{\partial u_z}{\partial x}\right)\frac{h}{U}, \tag{3.4}$$

where V is the volume of the flow field of interest. The enstrophies shown in figure 8(*b*) are integrated over the wake region of $x/h = 0$–20. In general, the degree of three-dimensionality increases gradually with increasing Re. In addition, the ε_x and ε_y values over the mode swapping regime are decomposed into the ones corresponding to the dislocation and non-dislocation periods. The enstrophies for the dislocation periods are slightly larger than those for the non-dislocation periods, which suggests that the dislocation periods have larger degrees of flow three-dimensionality than the non-dislocation periods. The larger degrees of flow three-dimensionality for the

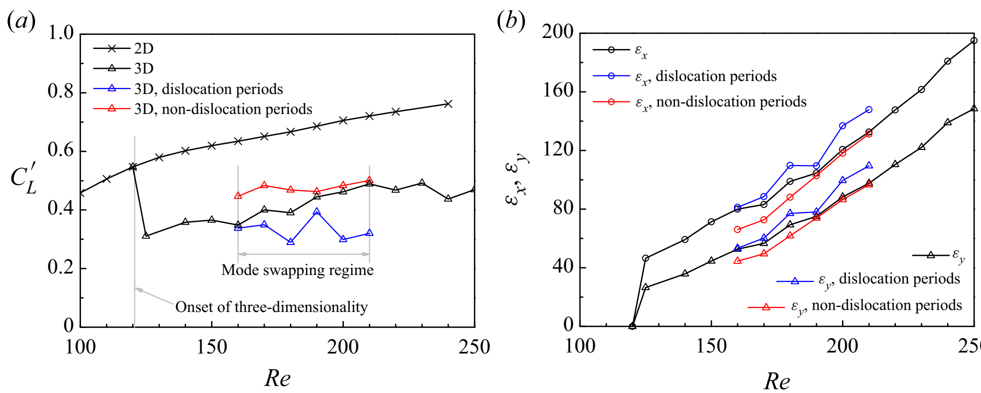

Figure 8. (*a*) The C_L'–*Re* relationship, and (*b*) the ε_x–*Re* and ε_y–*Re* relationships (integrated over $x/h = 0$–20) over the wake transition regimes.

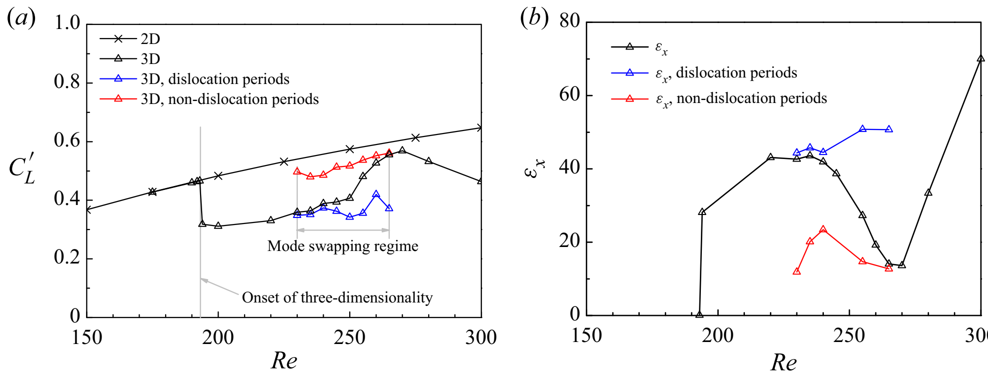

Figure 9. (*a*) The C_L'–*Re* relationship, and (*b*) the ε_x–*Re* relationship (integrated over $x/D = 0$–10) over the wake transition regimes for flow past a circular cylinder.

dislocation periods are consistent with the larger reductions in the C_L' values from their 2-D counterparts shown in figure 8(*a*).

In comparison, figure 9 shows the C_L'–*Re* and ε_x–*Re* relationships for flow past a circular cylinder. In the mode swapping regime of $Re \sim 230$–265 (Williamson 1996; Barkley *et al.* 2000; Sheard *et al.* 2003; Jiang *et al.* 2016), the C_L' and ε_x values corresponding to the dislocation and non-dislocation periods are calculated in the present study by further analysing the numerical cases reported by Jiang *et al.* (2016), where the dislocation and non-dislocation time periods are identified in a similar manner to figure 5. Similar to the diamond cylinder, for a circular cylinder the dislocation periods also display larger degrees of flow three-dimensionality and larger reductions in C_L' (from their 2-D counterparts) than the non-dislocation periods (figure 9).

However, a major difference between a circular and a diamond cylinder is that for a circular cylinder there is a critical condition at the upper end of the mode swapping regime (Williamson 1996), where a local peak or trough is observed for various flow properties (see e.g. figure 9). In contrast, such a critical condition does not appear for a diamond cylinder (figure 8). Such a difference between a circular and a diamond cylinder originates from the development of particularly ordered and parallel mode B structures for the non-dislocation periods of a circular cylinder (see e.g. figure 14(*c*) of Jiang *et al.* 2016) whereas more disordered mode B structures for the non-dislocation periods of a diamond cylinder (see e.g. figure 4*k*). For a circular cylinder, the particularly ordered mode B structures for the non-dislocation periods induce ε_x values less than half of those for the dislocation periods (figure 9*b*) and C_L' values very close to the largest possible level, i.e. their 2-D counterparts (figure 9*a*). In contrast, the disordered mode B structures observed for the non-dislocation periods of a diamond cylinder induce relatively large degrees of flow three-dimensionality comparable to those of the dislocation periods (figure 8*b*) and C_L' values much smaller than their 2-D counterparts (figure 8*a*). Since the non-dislocation branches shown in figure 8 are now closer to the dislocation branches than the 2-D curves (for figure 8*b* the 2-D results are $\varepsilon_x = \varepsilon_y = 0$), the overall C_L'–Re, ε_x–Re and ε_y–Re curves, which are bounded by the dislocation and non-dislocation branches, do not show obvious peak/trough towards their 2-D counterparts at the upper end of the mode swapping regime. Instead, only slight changes in the variation trends may be observed when the overall curve detaches the dislocation branch at $Re \sim 160$ and attaches the non-dislocation branch at $Re \sim 210$. These slight changes may easily be overlooked when the dislocation and non-dislocation branches are switched off.

3.3. *Vortex shedding frequency*

Figure 10 shows the frequency spectra of C_L for the determination of the vortex shedding frequency. The frequency spectra are obtained from the FFT of the time histories of C_L. Each frequency spectrum shown in figure 10 contains a main peak, accompanied by broadband frequencies at the two sides of the peak, owing to the irregularity of the 3-D flows.

Based on the separation of the time history of C_L into the dislocation and non-dislocation periods in figure 7, the frequency spectrum of C_L can also be decomposed by performing FFT separately on the dislocation and non-dislocation ranges of the time history. Figure 11(*a*) shows an example of the decomposition of the frequency spectrum of C_L for $Re = 180$. It is seen that the peak frequency corresponding to the non-dislocation periods is much closer to that of the dislocation periods than that calculated through 2-D DNS, which is similar to the variation trends of ε_x and ε_y shown in figure 8(*b*). Jiang & Cheng (2017) also showed based on a circular cylinder that in the mode swapping regime the degree of reduction in the 3-D St value from its 2-D counterpart correlates well with the degree of flow three-dimensionality. In comparison, figure 11(*b*) shows a circular cylinder example at $Re = 250$, where the peak frequency corresponding to the non-dislocation periods is much closer to its 2-D counterpart than that of the dislocation periods. For the circular cylinder, the difference between the peak frequencies corresponding to the dislocation and non-dislocation periods (of $\Delta St = 0.0104$) can be revealed by the frequency spectrum corresponding to the entire time history of C_L, where two peaks of $\Delta St = 0.00997$ apart are observed (figure 11*b*). For the diamond cylinder, however, because the difference between the peak frequencies corresponding to the dislocation and non-dislocation periods (of $\Delta St = 0.00195$) is even smaller than the range of St under the main frequency peak (of $\Delta St \gtrsim 0.005$), the frequency spectrum corresponding to the entire time history of C_L cannot display the twin-peaked pattern. The relatively small ΔSt between the dislocation and non-dislocation branches over the mode swapping regime can also be viewed in figure 10 by highlighting the peak frequencies of $Re = 150$ (just before mode swapping) and $Re = 220$ (just after mode swapping) using two vertical lines, where a similar minor difference of $\Delta St = 0.00318$ is observed.

Figure 12 shows the St–Re relationship over the wake transition regimes for flow past a diamond cylinder. At the onset of three-dimensionality, a sudden drop in the St value

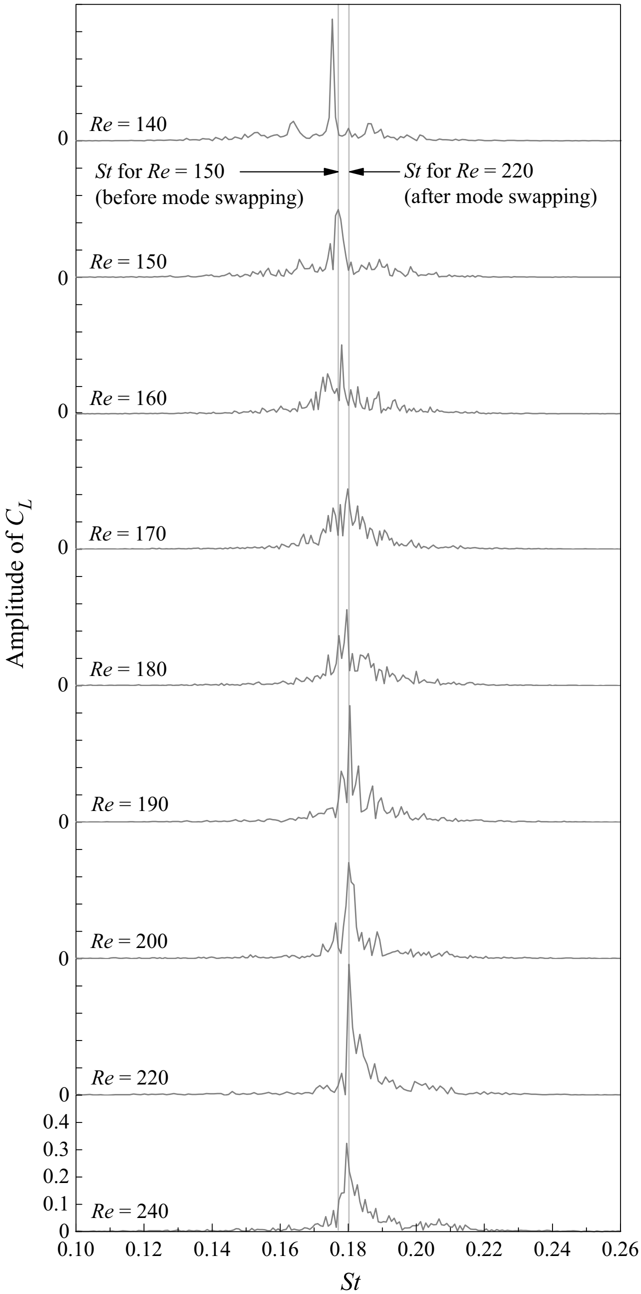

Figure 10. Frequency spectra of C_L for $Re = 140$–240.

(of 5.6%) is observed, which, according to Jiang *et al.* (2018*a*), is consistent with the subcritical nature of the mode A instability for a diamond cylinder (Sheard *et al.* 2009) and the associated sudden increase in the degree of flow three-dimensionality at Re_{cr} (figure 8*b*). For $Re > Re_{cr}$, a continuous *St*–*Re* relationship is observed for the 3-D flows, including the mode swapping regime highlighted in figure 12, since the twin-peaked pattern is not observed for the frequency spectra shown in figure 10.

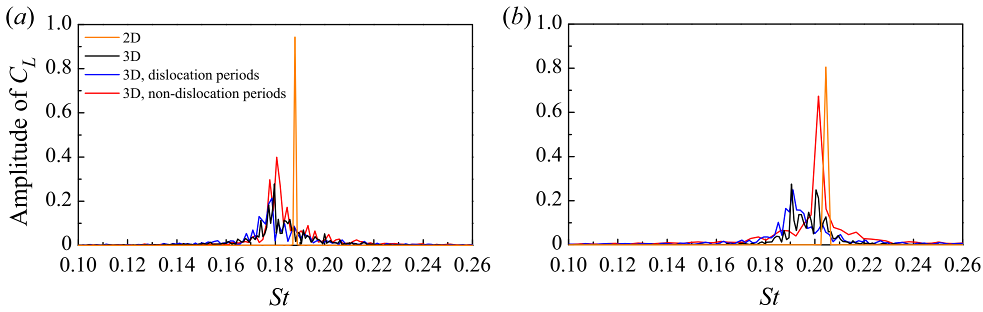

Figure 11. Frequency spectra of C_L for (*a*) flow past a diamond cylinder at $Re = 180$, and (*b*) flow past a circular cylinder at $Re = 250$.

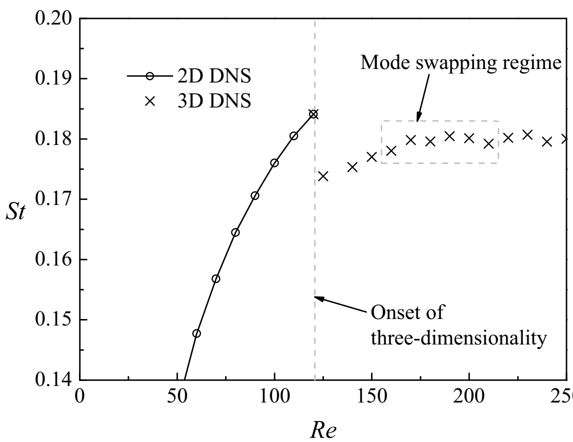

Figure 12. The *St*–*Re* relationship over the wake transition regimes.

3.4. *The drag coefficient*

Figure 13 shows the $\overline{C_D}$–*Re* relationship over the wake transition regimes. In addition, the total drag coefficient is decomposed into the pressure and viscous components. The present 2-D results agree relatively well with those reported by Yoon *et al.* (2010). As *Re* exceeds the onset of the primary wake instability, the pressure drag starts to increase while the viscous drag continues to decrease, which is similar to that of a circular cylinder investigated in Henderson (1995). However, a difference to a circular cylinder (Henderson 1995) or a square cylinder (Jiang & Cheng 2018) is that for a diamond cylinder the increase rate of the pressure drag is larger than the decrease rate of the viscous drag, such that the total drag exhibits an increase right after the onset of the primary wake instability. At the onset of the secondary wake instability, both the pressure and viscous drag display an approximately 7% decrease, which is consistent with the sudden decrease/increase in *St* (figure 12), C_L' (figure 8*a*) and the degree of flow three-dimensionality (figure 8*b*) discussed in §§ 3.2 and 3.3.

Based on the decomposition of the pressure and viscous drag coefficients (denoted $\overline{C_{D,p}}$ and $\overline{C_{D,v}}$, respectively) in figure 13, the ratio between the pressure drag and the total drag ($\overline{C_{D,p}}/\overline{C_D}$) is quantified in figure 14. In comparison, figure 14 also shows the results for a circular cylinder, a square cylinder (with $\alpha = 0\,^{\circ}$) and inclined square cylinders with $\alpha = 15.3\,^{\circ}$ and $29.7\,^{\circ}$, based on the $\overline{C_{D,p}}$ and $\overline{C_{D,v}}$ values reported by Jiang

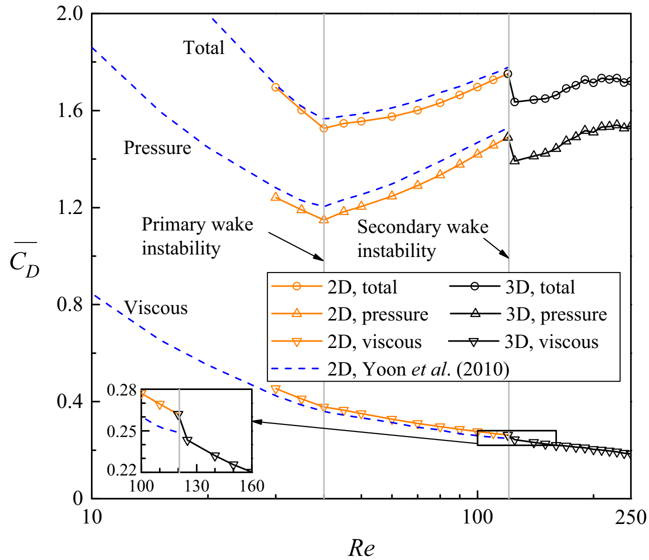

Figure 13. The $\overline{C_D}$–Re relationship over the wake transition regimes.

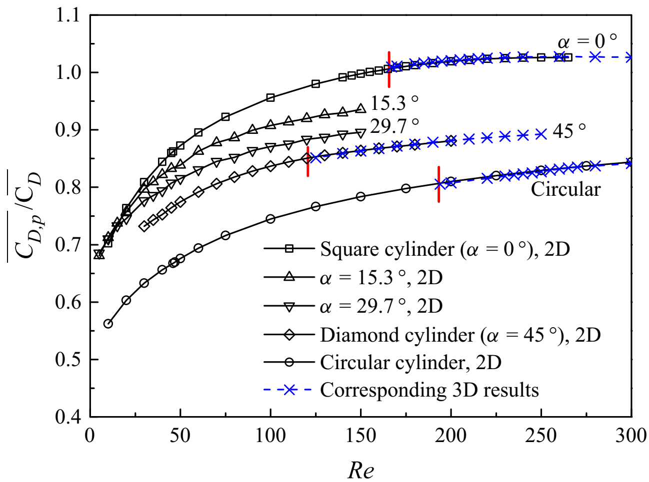

Figure 14. The ratio between the pressure drag and the total drag for different cylinders. The red vertical bars indicate the onset of three-dimensionality.

& Cheng (2018) and Yoon *et al.* (2010). The red vertical bars in figure 14 indicate the onset of three-dimensionality for circular, square and diamond cylinders, where the 3-D results appear to the right of them. In addition, the 2-D simulations have been extended beyond the onset of three-dimensionality (although unphysical in real situations), and the 2-D results show excellent agreement with the corresponding 3-D results. The agreement between the 2-D and 3-D results is attributed to a very similar percentage decrease in the pressure and viscous drag at the onset of three-dimensionality (e.g. figure 13). Therefore, the 2-D results for $\alpha = 15.3\,^{\circ}$ and $29.7\,^{\circ}$ can be used without having to consider the effect of three-dimensionality.

A common feature for the cylinders investigated in figure 14 is that, for each cross-sectional shape, the projected length perpendicular to the incoming flow (which contributes to the pressure drag) is the same as the projected length parallel to the incoming flow (which contributes to the viscous drag). Therefore, the ratio $\overline{C_{D,p}}/(\overline{C_{D,p}} + \overline{C_{D,v}}) = \overline{C_{D,p}}/\overline{C_D}$ serves as a direct indication of the bluffness of the cylinder. As shown in figure 14, the $\overline{C_{D,p}}/\overline{C_D}$ value, and hence the bluffness of the cylinder, is largest for a square cylinder, followed by inclined square cylinders with increasing α from $0°$ to $45°$, and smallest for a circular cylinder.

3.5. *Floquet analysis of the 3-D wake instability modes*

As discussed in § 3.1, the mode B structures observed at $Re \geq 150$ are destabilised by the mode A structures that exist in the wake. On the other hand, it is also of interest to examine the global instability of mode B (and other modes) to the 2-D base flow, where the interactions between the modes A and B structures are eliminated. In general, Floquet stability analysis has been a preferred method in determining the 3-D modes that are unstable to the 2-D base flow, e.g. the mode B instability of a circular cylinder (Barkley & Henderson 1996; Posdziech & Grundmann 2001) and a square cylinder (Robichaux *et al.* 1999; Sheard *et al.* 2009; Park & Yang 2016), among many others. A necessary condition for the use of the Floquet analysis is that the 2-D base flow is time periodic (Barkley & Henderson 1996). For a diamond cylinder, however, Sheard *et al.* (2009) found that the 2-D base flow became aperiodic at $Re \gtrsim 140$, such that no Floquet analysis had been performed for $Re \gtrsim 140$ to identify the instability modes other than mode A.

In the present study, the 3-D instability modes of a diamond cylinder for $Re \gtrsim 140$ are examined by the Floquet analysis with caution. The aperiodicity of the 2-D base flow is illustrated in figure 15(*a*,*b*) at $Re = 300$ with two instantaneous vorticity fields of one primary vortex shedding period ($T^* = TU/h$) apart, where the vorticity fields become aperiodic at $x/h \gtrsim 7$. In addition, figure 15(*c*) shows the locations of the vortex centres extracted from 19 snapshots of the vorticity field (including the vorticity field shown in figure 15*a*), which illustrates more clearly that the wake becomes aperiodic at $x/h \gtrsim 7$. The two vertical dashed lines in each panel of figure 15 mark the streamwise locations where the wake transitions from the primary vortex street to the two-layered and the secondary vortex streets. The transition locations are determined as the x/h values corresponding to the local maxima in the time-averaged transverse velocity field shown in figure 15(*d*) (Jiang & Cheng 2019). A mesh convergence check conducted at $Re = 300$ (the largest Re considered by the Nektar++ model used in this section) shows that an increase in N_p from 5 to 7 results in variations in the two transition locations of 0.5%, which suggests that the use of $N_p = 5$ is adequate. As shown in figure 15(*a*–*c*), the wake remains periodic when the primary vortices rearrange themselves to the two-layered pattern, while the wake gradually becomes aperiodic when the two-layered vortices rearrange themselves for the irregular vortex merging (see e.g. figure 15*b*) at the transition to the secondary vortex street. In other words, the aperiodicity of the 2-D base flow arises from the transition from the two-layered to the secondary vortex street. Such a transition is not observed for $Re = 140$ within the wake domain length up to $x/h = 40$ (and the entire wake is perfectly periodic), but is observed for $Re \geq 160$ (and the wake is aperiodic), such that the Floquet analysis of $Re \geq 160$ should be conducted with caution.

Figure 16 shows the $|\mu|-\beta$ relationships for $Re = 300$, predicted through the Floquet analysis using two different vortex shedding periods of the base flows, i.e. $t^* = 1400 - (1400 + T^*)$ and $t^* = 1600 - (1600 + T^*)$. It is found that the aperiodicity

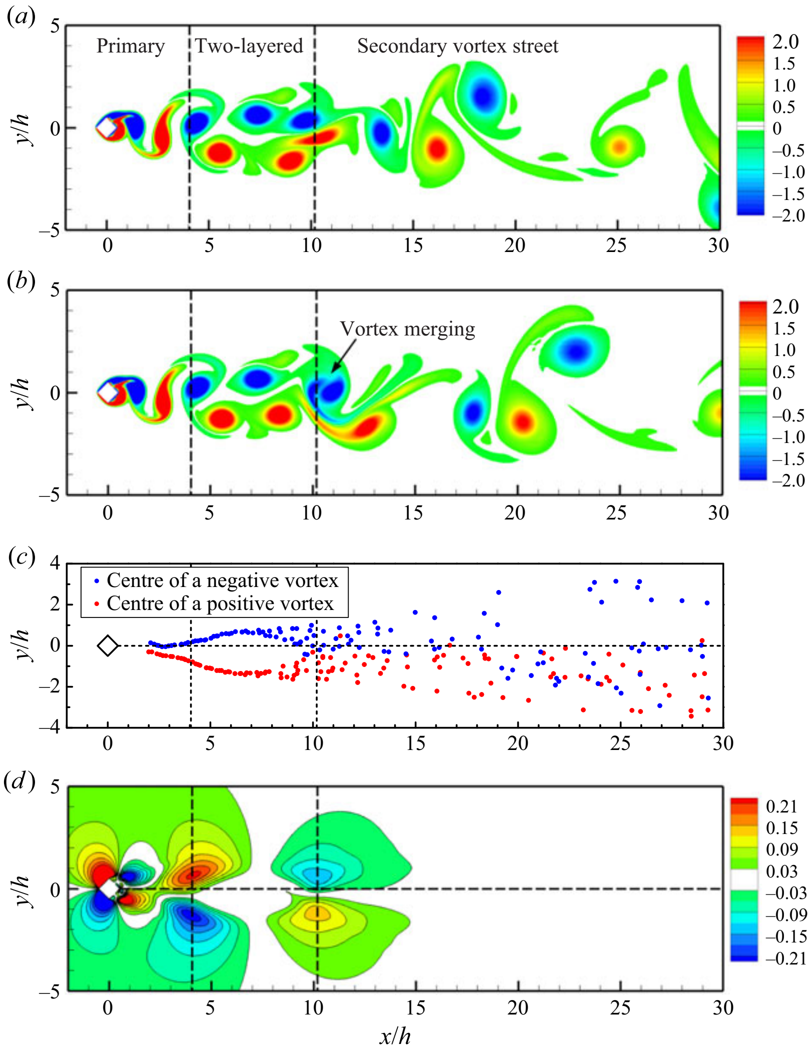

Figure 15. Characteristics of the 2-D base flow for $Re = 300$: (*a*) instantaneous vorticity field at $t^* = 1400$, (*b*) instantaneous vorticity field at $t^* = 1400 + T^*$, (*c*) locations of the vortex centres extracted from 19 snapshots of the vorticity field (at $t^* = 1000$ to 2800 with an interval of 100) and (*d*) time-averaged transverse velocity field. The vertical dashed lines mark the two transition locations, while the horizontal dashed line in panels (*c*,*d*) marks the wake centreline.

of the base flow results in quantitative uncertainties in the $|\mu|-\beta$ relationship, while, qualitatively, the unstable peaks (i.e. the wake instability modes) are the same. The first peak at $\beta h \sim 0.8$–1.8 contains real and positive μ values, which correspond to the mode A instability. The second peak at $\beta h \sim 2.8$–4 contains real and negative μ values, which correspond to a subharmonic mode. Based on further computations, the critical Re for the instability of the subharmonic mode is located within 280–285. Other than these two modes, no additional instability modes are identified by the Floquet analysis over $Re = 120$–300 (with an interval of 20).

To eliminate the quantitative uncertainties in the $|\mu|-\beta$ relationship induced by the aperiodicity of the base flow, phase-averaged (hence T-periodic) base flow is attempted

https://doi.org/10.1017/jfm.2021.354 Published online by Cambridge University Press

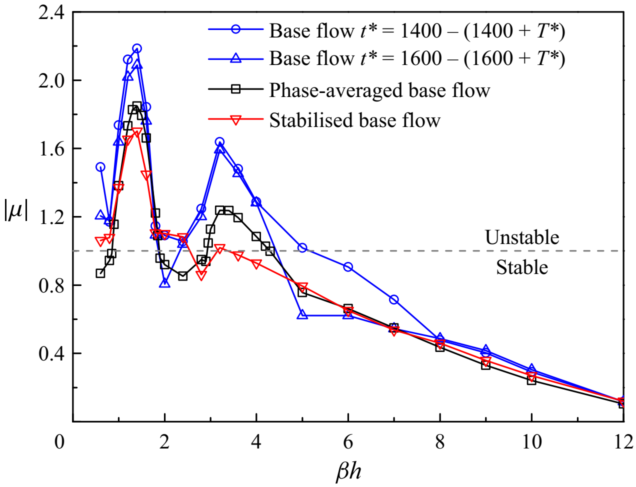

Figure 16. The $|\mu|-\beta$ relationships for $Re = 300$, predicted through the Floquet analysis using different base flows. The horizontal dashed line marks the neutral instability of $|\mu| = 1.0$.

for the Floquet analysis. The phase-averaged base flow is generated based on $200T$ of the fully developed original 2-D flow. Figure 17(a,b) illustrates the phase-averaged base flow for $Re = 300$ at two phases of $T/2$ apart. The $|\mu|-\beta$ relationship predicted using the phase-averaged base flow is also shown in figure 16, where, similarly, a mode A and a subharmonic mode are obtained, which suggests again that the aperiodicity of the base flow induces a quantitative but not qualitative influence on the Floquet instability modes. Based on the phase-averaged base flow, Floquet analyses were performed for $Re \geq 160$. Figure 18 shows the extended neutral instability curve for mode A up to $Re = 300$ (cf. figure 3b). In addition, the subharmonic instability mode is identified at $Re \geq 285$.

To further confirm the existence of the subharmonic instability mode predicted by the Floquet analysis, 3-D DNS were conducted using $L_z/h = 1$–3 to eliminate the influence of mode A and to reveal the relatively small-scale subharmonic instability mode. The present DNS cases and their 2-D or 3-D near-wake patterns are summarised in figure 18 using isolated symbols. The DNS results agree well with the neutral instability curves. For $Re = 260$ and 280, the near wake becomes three-dimensional when L_z/h increases from 2.5 to 3, and the wake of $L_z/h = 3$ is represented by one spanwise period of the mode A structure. For $Re = 290$, the near wake first becomes three-dimensional when L_z/h increases from 1.4 to 1.5, and the near wake is represented by one spanwise period of the subharmonic mode. The subharmonic mode observed at $L_z/h = 1.5$ is free from the influence of mode A that may appear at larger L_z/h values. The existence of the subharmonic instability mode is thus cross-checked by both DNS and the Floquet analysis, where both methods predict its onset of instability at Re within 280–290.

The subharmonic mode is also observed at $Re = 300$ when L_z/h increases from 1.3 to 1.4. The subharmonic mode at $Re = 300$ and $L_z/h = 1.4$ is investigated in detail by examining the instantaneous ω_z and ω_x fields over a period of $20T$. Figure 19 illustrates the ω_z (a,c,e) and ω_x (b,d,f) fields at the plane $z/h = 0.1$ over a period of $2T$. Panels (a,b) of figure 19 are shown at an arbitrary time instant in the fully developed flow, while panels (c,d) and (e,f) are shown at time evolutions of T and $2T$, respectively. It is seen that the ω_z fields shown in figure 19(a,c,e) are generally T-periodic at $x/h \lesssim 7$, which is similar to those of the 2-D flow shown in figure 15(a,b). However, while the $|\omega_x|$ fields in figure 19(b,d,f) are

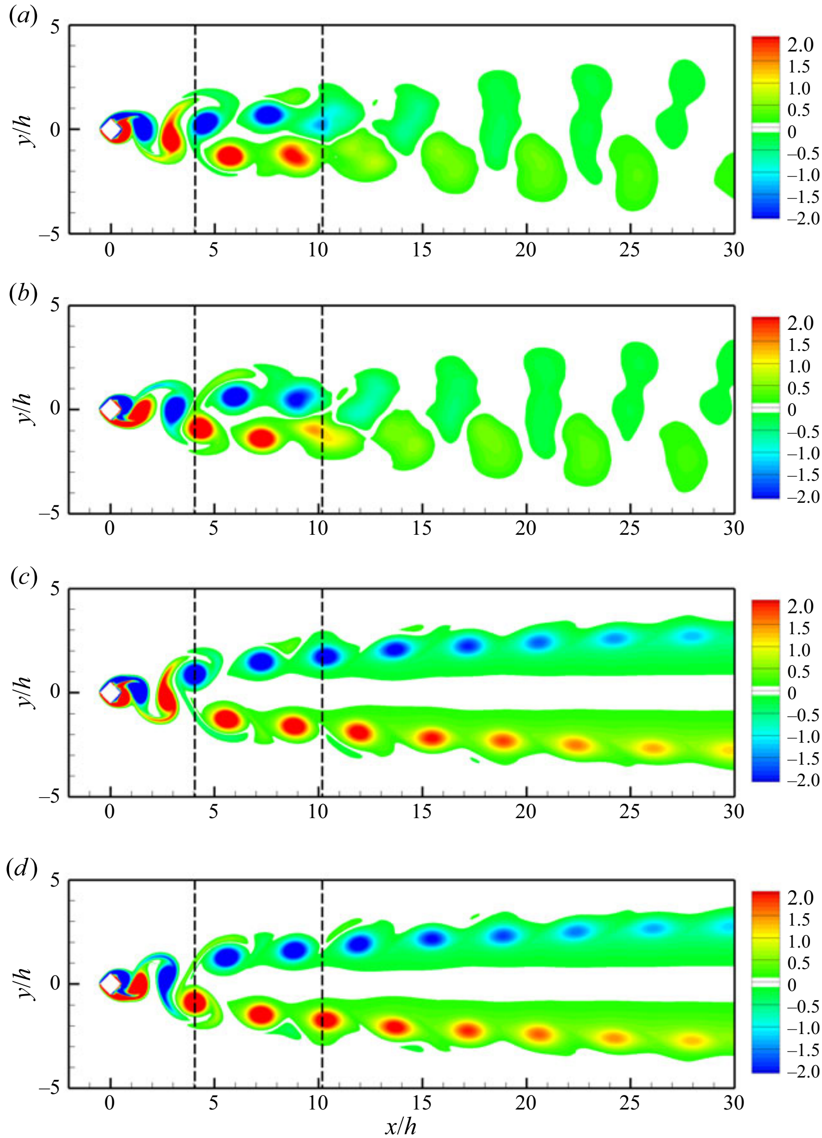

Figure 17. Illustration of T-periodic base flows for $Re = 300$. Panels (a,b) show instantaneous vorticity fields for the phase-averaged base flow at two phases of $T/2$ apart, while panels (c,d) show instantaneous vorticity fields for the stabilised base flow at two phases of $T/2$ apart. The base flows in panels (a,c) are shown at the same phase as figure 15(a,b). The vertical dashed lines mark the two transition locations for the original aperiodic 2-D flow.

generally T-periodic at $x/h \lesssim 7$, the streamwise vortices change sign every T, resulting in the period doubling of the flow.

The physical mechanism for the development of the subharmonic mode is investigated below. It is anticipated that the development of the subharmonic mode is related to the development of the secondary vortex street relatively close to the cylinder. To prove this point, an additional Floquet analysis was conducted by using a base flow without the transition to the secondary vortex street. The transition to the secondary vortex street can

https://doi.org/10.1017/jfm.2021.354 Published online by Cambridge University Press

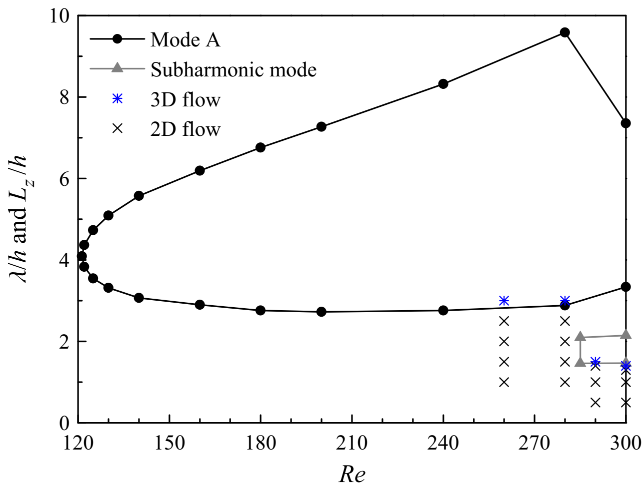

Figure 18. The neutral instability curves for mode A and the subharmonic mode. The Floquet analyses for $Re \geq 160$ are performed based on the phase-averaged base flow.

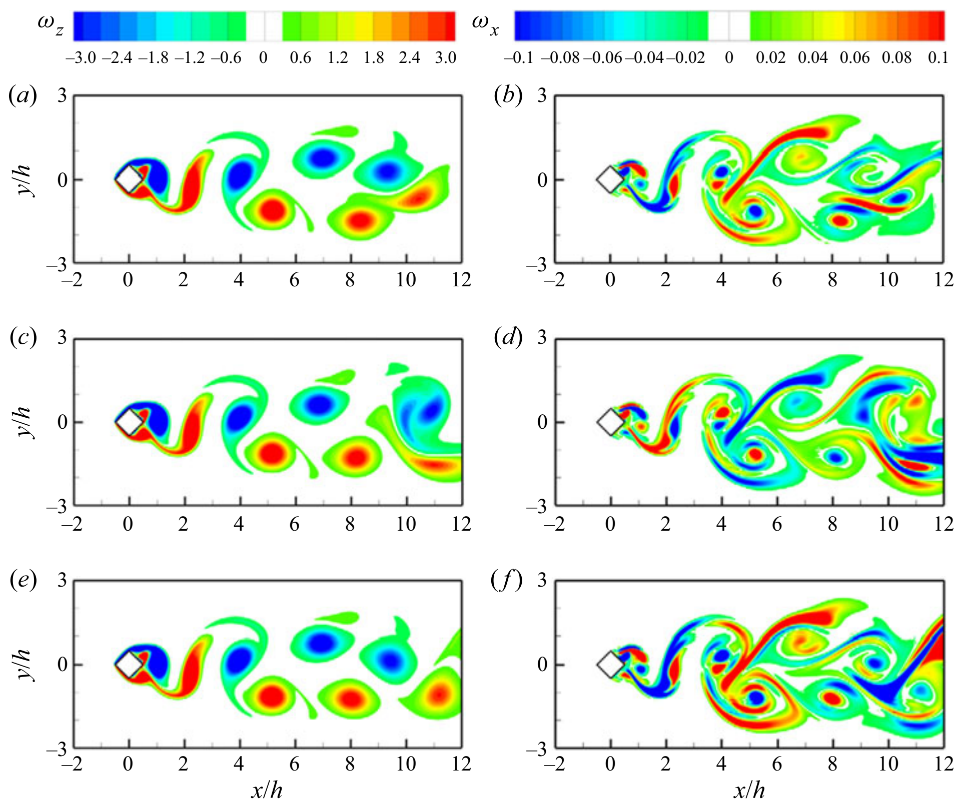

Figure 19. Instantaneous ω_z (*a,c,e*) and ω_x (*b,d,f*) fields at the plane $z/h = 0.1$ for the 3-D DNS case of $Re = 300$ and $L_z/h = 1.4$. Panels (*a,b*) are shown at an arbitrary time instant in the fully developed flow, while panels (*c,d*) and (*e,f*) are shown at time evolutions of T and $2T$, respectively.

be suppressed by stabilising the two-layered vortex street until the outlet boundary (see figure 17*c*,*d*) through the following procedures:

(i) Compute the fully developed 2-D flow and the corresponding vortex shedding period T.
(ii) Repeat the following until the two-layered vortex street is stabilised till the outlet: advance the flow by a period of T and use the average of the flow fields at the beginning and the end of the T-period as the initial condition for the next iteration.
(iii) Compute the updated T for the stabilised flow field.
(iv) Repeat steps (ii) and (iii) until the updated T does not change.

It is worth noting that the stabilised base flow is strictly T-periodic, since the aperiodic transition to the secondary vortex street is suppressed.

Based on the stabilised base flow, the $|\mu|-\beta$ relationship for $Re = 300$ is also shown in figure 16. While the first peak at $\beta h \sim 0.8$–1.8 still corresponds to the mode A instability, the second peak, which is marginally unstable at $\beta h = 3.2$ with a real and positive μ value (rather than a real and negative μ for the subharmonic mode), corresponds to a wake instability in the two-layered vortex street near the outlet, which would not exist in the original base flow.

The disappearance of the subharmonic mode in the stabilised base flow sheds light on the origin of the subharmonic mode. For the original base flow (and naturally also the phase-averaged base flow), it is found that the time-averaged flow becomes asymmetric about the wake centreline at $Re \geq 285$ (e.g. figure 15*d*). Consistently, the time-averaged lift coefficient becomes non-zero, the trajectories for the positive and negative vortices become asymmetric about the wake centreline (figure 15*c*) and the corresponding phase-averaged base flow (figure 17*a*,*b*) breaks the following spatio-temporal symmetry:

$$\omega_z(x, y, t) = -\omega_z(x, -y, t + T/2). \tag{3.5}$$

Physically, subharmonic modes are often detected by the Floquet analysis when the base flow breaks the above spatio-temporal symmetry (Blackburn & Sheard 2010), even when the bluff body and the incoming flow are symmetric about the wake centreline (e.g. Serson *et al.* 2014). Therefore, it is not surprising that the critical Re for the asymmetry of the time-averaged flow coincides with the critical Re for the instability of the subharmonic mode (both at $Re = 280$–285). In contrast, the stabilised base flow (figure 17*c*,*d*) possesses the spatio-temporal symmetry given in (3.5), such that no subharmonic mode is detected by the Floquet analysis. A comparison between the original/phase-averaged base flow and the stabilised base flow suggests that the breaking of the spatio-temporal symmetry described in (3.5) is induced by the transition to the secondary vortex street relatively close to the cylinder, which rearranges the near-wake vortex pattern upstream of the transition.

Although the subharmonic mode is detected by the Floquet analysis and 3-D DNS with L_z smaller than the spanwise wavelengths of mode A at $Re \gtrsim 285$, it may not exist in the natural 3-D flow. Instead, § 3.1 shows that the mode B structures are observed in the natural 3-D flow at $Re \geq 150$ and dominate the wake at $Re \geq 220$, although none of the Floquet analysis conducted here detects the mode B instability. In addition, table 2 summarises the wake structures for $Re = 300$ predicted by the 3-D DNS under different L_z/h constraints. A mesh convergence check was performed for the case $L_z/h = 12$ by increasing N_p from 5 to 6, where the St, $\overline{C_D}$ and C_L' values vary by less than 1%. It is seen in table 2 that with increasing L_z/h from 3 to 6, the wake structure changes from the ordered subharmonic mode (figure 20*a*) to disordered mode B (figure 20*b*). The existence of mode B rather than the subharmonic mode for $L_z/h = 6$ and 12 is supported by the following evidence.

L_z/h	Streamwise vortices	Spanwise vortices	$\lvert\overline{C_L}\rvert$
0	n/a	Ordered	0.037
1.4	One spanwise period of the ordered subharmonic mode	Ordered	0.032
1.5	One spanwise period of the ordered subharmonic mode	Ordered	0.029
3	Two spanwise periods of the ordered subharmonic mode (Figure 20*a*)	Ordered (Figure 20*a*)	0.029
6	Disordered mode B (Figure 20*b*)	Disordered (Figure 20*b*)	$O(10^{-4})$
12	Disordered mode B	Disordered	$O(10^{-4})$

Table 2. Wake structures for $Re = 300$ predicted by the 3-D DNS under different L_z/h constraints.

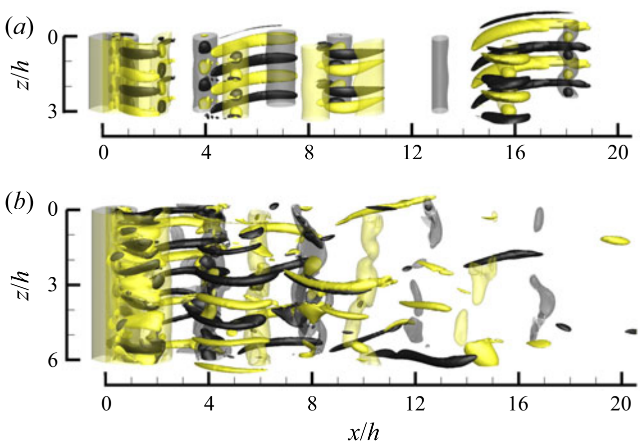

Figure 20. Instantaneous vorticity fields for $Re = 300$ predicted by the 3-D DNS using (*a*) $L_z/h = 3$ and (*b*) $L_z/h = 6$. The translucent iso-surfaces represent spanwise vortices with $\omega_z = \pm 2$, while the opaque iso-surfaces represent streamwise vortices with $\omega_x = \pm 0.4$ for panel (*a*) and $\omega_x = \pm 2$ for panel (*b*). Dark grey and light yellow denote positive and negative vorticity values, respectively. The flow is from left to right past the cylinder on the left.

(i) The streamwise vortices possess the spatio-temporal symmetry corresponding to mode B rather than the subharmonic mode.
(ii) The time-averaged lift coefficient is practically zero (of the order of 10^{-4}).
(iii) The mode B structures emerge at $Re \geq 150$, which is much smaller than the onset of the subharmonic mode at $Re \sim 285$.

The development of mode B rather than the subharmonic mode in the natural 3-D flow is attributed to the influence of the mode A instability. The mode A streamwise vortices may destabilise mode B through (i) destabilising the braid shear layer region (Jiang *et al.* 2016) for the hyperbolic instability of mode B (Williamson 1996; Leweke & Williamson 1998; Thompson *et al.* 2001), and (ii) modulating the pattern of the spanwise vortices (i.e. the base flow) to allow for the instability of mode B. To demonstrate the latter mechanism, the span-averaged spanwise vorticity fields for $Re = 300$ computed with $L_z/h = 3$ and 6 are shown in figure 21. For $L_z/h = 3$, the ordered streamwise vortices of the subharmonic mode do not induce noticeable influence on the spanwise vortices (figure 20*a*), such that the pattern of the spanwise vortices shown in figure 21(*a*) is similar to that computed with

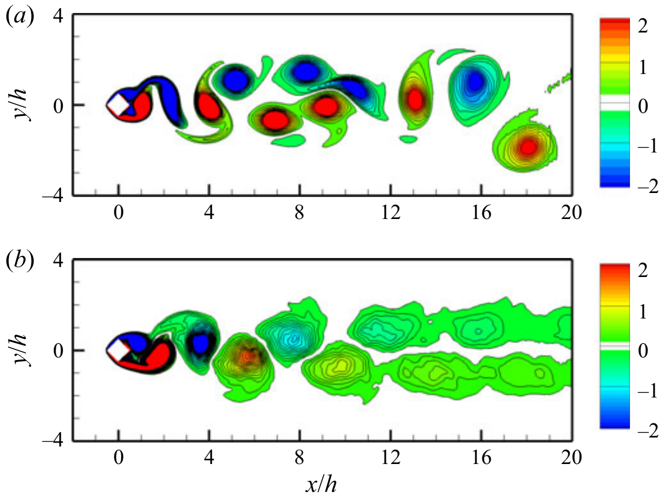

Figure 21. Span-averaged spanwise vorticity fields for $Re = 300$, obtained from (*a*) the instantaneous 3-D flow field shown in figure 20(*a*) computed with $L_z/h = 3$, and (*b*) the phase-averaged 3-D flow computed with $L_z/h = 6$.

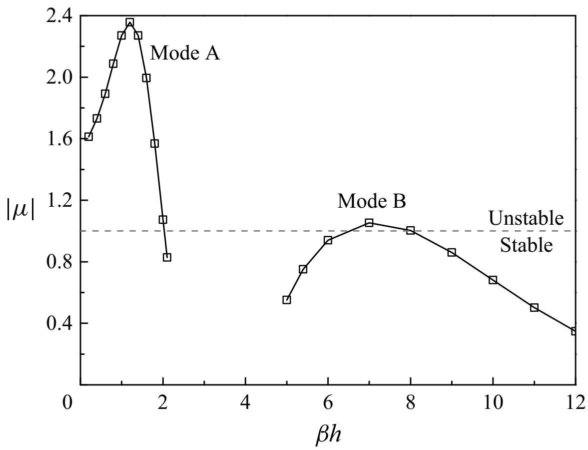

Figure 22. The $|\mu|-\beta$ relationship for $Re = 300$, predicted through the Floquet analysis using the modulated base flow. The horizontal dashed line marks the neutral instability of $|\mu| = 1.0$.

2-D DNS (figure 15*a*,*b*), where the primary vortex street transitions to the two-layered and secondary vortex streets at $x/h \sim 4$ and 10, respectively. For $L_z/h = 6$, the spanwise vortices are highly disordered (figure 20*b*), such that the spanwise vorticity field shown in figure 21(*b*) is based on a phase average over 25 vortex shedding cycles. Compared with figure 21(*a*), the pattern and strength of the spanwise vortices shown in figure 21(*b*) are significantly modulated by the disordered streamwise vortices (figure 20*b*) and the associated development of turbulence and turbulent dissipation.

It is anticipated that the modulated pattern of the spanwise vortices may give rise to the instability of mode B. Therefore, an additional Floquet analysis is conducted, where the base flow is the phase- and span-averaged spanwise vorticity fields for $Re = 300$ obtained with $L_z/h = 6$ (called the modulated base flow hereafter). Figure 22 shows the $|\mu|-\beta$

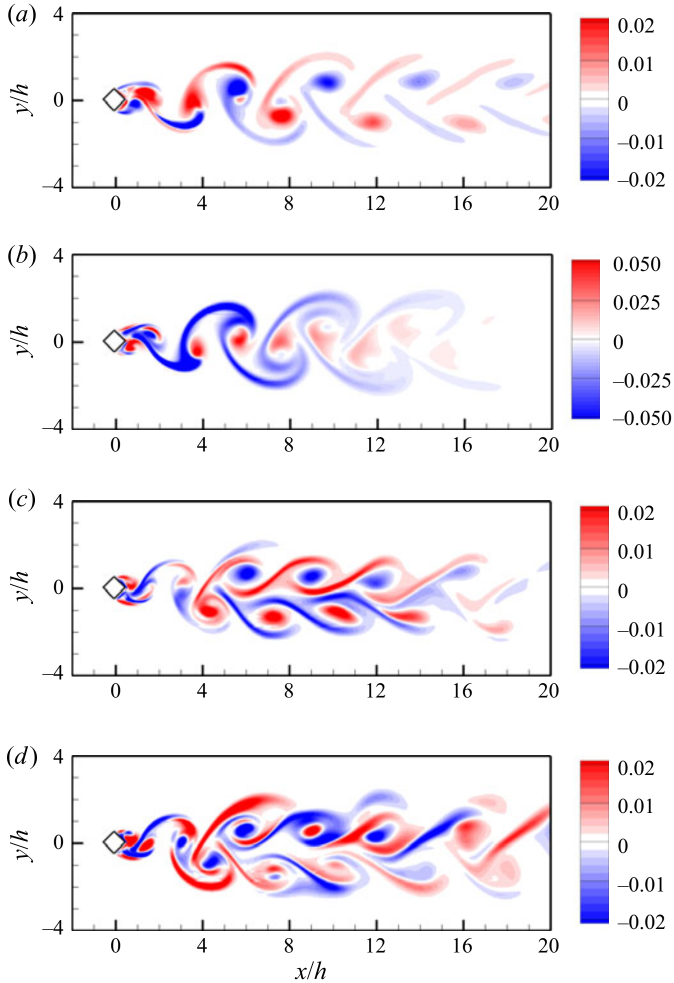

Figure 23. Streamwise perturbation vorticity fields for $Re = 300$: (*a*) mode A predicted by $\beta h = 1.8$ of the modulated base flow, (*b*) mode B predicted by $\beta h = 7$ of the modulated base flow, (*c*) mode A predicted by $\beta h = 1.4$ of the phase-averaged base flow and (*d*) the subharmonic mode predicted by $\beta h = 3.2$ of the phase-averaged base flow. Red and blue denote positive and negative vorticity values, respectively.

relationship for $Re = 300$, predicted through the Floquet analysis using the modulated base flow. The two unstable modes identified in figure 22 both contain real and positive μ values, which correspond to synchronous modes. The streamwise perturbation vorticity fields for the two modes are shown in figure 23(*a*,*b*). The perturbation patterns of the two modes agree well with those for modes A and B for circular and square cylinders (see e.g. Robichaux *et al.* 1999; Carmo, Meneghini & Sherwin 2010). The most unstable spanwise wavelength for mode B ($\sim 0.9h$) is similar to the wavelengths for mode B for circular and square cylinders (Barkley & Henderson 1996; Choi *et al.* 2012; Park & Yang 2016).

For completeness, figure 23(*c*,*d*) shows the streamwise perturbation vorticity fields for mode A and the subharmonic mode predicted with the phase-averaged base flow illustrated in figure 17(*a*,*b*). For mode A, the perturbation structure displays opposite signs for the two sides of the wake centreline (figure 23*a*,*c*). For the subharmonic mode, the perturbation structure displays both signs alternately at each side of the wake centreline (figure 23*d*).

The most unstable spanwise wavelength for the subharmonic mode ($\sim$1.9h) is similar to the wavelengths for the subharmonic mode observed in the wake of other bluff bodies (e.g. Sheard *et al.* 2009; Yildirim, Rindt & van Steenhoven 2013).

However, figure 22 shows that the subharmonic mode is suppressed by the modulated pattern of the spanwise vortices shown in figure 21(*b*). As discussed earlier in this section, the subharmonic mode is unstable to the original and phase-averaged base flows where the spatio-temporal symmetry described in (3.5) is broken by the transition to the secondary vortex street relatively close to the cylinder. For the modulated base flow shown in figure 21(*b*), the two-layered vortices with significantly weakened vorticity do not transition to the secondary vortex street, and the wake possesses the spatio-temporal symmetry (see e.g. the $|\overline{C_L}|$ values in table 2), such that the subharmonic mode is suppressed.

4. Conclusions

This paper investigates numerically the 3-D wake transition process of a diamond cylinder. Detailed 3-D DNS show that the wake becomes three-dimensional at $Re_{cr} \sim 121$ and is represented by mode A with global vortex dislocations for $Re = Re_{cr} - 150$. For $Re = 160$–210, a mode swapping between modes A and B takes place. With the increase in Re, the mode B structures are increasingly likely destabilised by the streamwise vortices of mode A, and consequently the probability of occurrence of mode A with global vortex dislocations decreases monotonically. For $Re \geq 220$, the wake is dominated by increasingly disordered mode B structures.

For the mode swapping regime, the different characteristics of the dislocation and non-dislocation periods are analysed quantitatively through a new approach. Specifically, a specific flow property (e.g. C_L', ε_x, ε_y, St, etc.) can be decomposed into the values corresponding to the dislocation and non-dislocation time periods. Owing to the vortex dislocations, the C_L' and St values for the dislocation periods are smaller than their counterparts for the non-dislocation periods, and consistently the ε_x and ε_y values (i.e. the degree of flow three-dimensionality) show the opposite. Quantitatively, the C_L', ε_x, ε_y and St values for the non-dislocation periods are closer to those for the dislocation branch than their 2-D counterparts. Therefore, the overall C_L'–Re, ε_x–Re and ε_y–Re curves, which are bounded by the dislocation and non-dislocation branches, display only slight changes in the variation trends when the overall curve detaches the dislocation branch at $Re \sim 160$ and attaches the non-dislocation branch at $Re \sim 210$. In addition, the relatively close St values for the dislocation and non-dislocation periods cannot be distinguished as two peaks in the overall frequency spectrum.

In contrast, a similar analysis for the circular cylinder case shows that the non-dislocation branch is much closer to the 2-D curve than the dislocation branch, such that the overall curve displays an obvious peak/trough towards its 2-D counterpart at the upper end of the mode swapping regime, commonly known as a critical condition (Williamson 1996). In addition, the St values for the dislocation and non-dislocation periods are now sufficiently apart to be distinguished as two peaks in the overall frequency spectrum.

In addition to DNS, Floquet stability analyses are conducted to identify the 3-D wake instability modes of a diamond cylinder up to $Re = 300$. Phase-averaged base flow is adopted to eliminate the quantitative uncertainties induced by the aperiodic secondary vortex street in the base flow. In addition to mode A, a subharmonic instability mode is identified at $Re \geq 285$, whereas mode B is not detected. The subharmonic instability mode is induced by the breaking of the Z_2 spatio-temporal symmetry of the base flow, which is further induced by the transition to the secondary vortex street relatively close to the cylinder and rearrangement of the near-wake vortex pattern upstream of the transition.

The disagreement between the natural 3-D flow and the Floquet analysis regarding the existence of mode B and the subharmonic mode is explained. For the natural 3-D flow, the existence of mode A modulates the pattern of the spanwise vortices (i.e. the base flow), which gives rise to the instability of mode B. In addition, the base flow modulated by the existence of modes A and B does not transition to the secondary vortex street, which suppresses the subharmonic mode. In summary, the natural 3-D flow involves complex interactions between the streamwise and spanwise vortices, as well as between the 3-D wake transition and the 2-D base-flow transition.

Funding. The author would like to acknowledge the support from the Australian Research Council through the DECRA scheme (Grant No. DE190100870). This work was supported by resources provided by the Pawsey Supercomputing Centre with funding from the Australian Government and the Government of Western Australia.

Declaration of interests. The author reports no conflict of interest.

Author ORCIDs.
Hongyi Jiang https://orcid.org/0000-0002-0137-6355.

References

Akbar, T., Bouchet, G. & Dušek, J. 2011 Numerical investigation of the subcritical effects at the onset of three-dimensionality in the circular cylinder wake. *Phys. Fluids* **23**, 094103.

Barkley, D. & Henderson, R.D. 1996 Three-dimensional Floquet stability analysis of the wake of a circular cylinder. *J. Fluid Mech.* **322**, 215–241.

Barkley, D., Tuckerman, L.S. & Golubitsky, M. 2000 Bifurcation theory for three-dimensional flow in the wake of a circular cylinder. *Phys. Rev.* E **61**, 5247–5252.

Blackburn, H.M. & Lopez, J.M. 2003 On three-dimensional quasiperiodic Floquet instabilities of two-dimensional bluff body wakes. *Phys. Fluids* **15**, L57–L60.

Blackburn, H.M. & Sheard, G.J. 2010 On quasiperiodic and subharmonic Floquet wake instabilities. *Phys. Fluids* **22**, 031701.

Cantwell, C.D., *et al.* 2015 Nektar++: an open-source spectral/hp element framework. *Comput. Phys. Commun.* **192**, 205–219.

Carmo, B.S., Meneghini, J.R. & Sherwin, S.J. 2010 Secondary instabilities in the flow around two circular cylinders in tandem. *J. Fluid Mech.* **644**, 395–431.

Choi, C., Jang, Y. & Yang, K. 2012 Secondary instability in the near-wake past two tandem square cylinders. *Phys. Fluids* **24**, 024102.

Henderson, R.D. 1995 Details of the drag curve near the onset of vortex shedding. *Phys. Fluids* **7**, 2102–2104.

Henderson, R.D. 1997 Nonlinear dynamics and pattern formation in turbulent wake transition. *J. Fluid Mech.* **352**, 65–112.

Henderson, R.D. & Barkley, D. 1996 Secondary instability in the wake of a circular cylinder. *Phys. Fluids* **8**, 1683–1685.

Issa, R.I. 1986 Solution of implicitly discretized fluid flow equations by operator-splitting. *J. Comput. Phys.* **62**, 40–65.

Jiang, H. & Cheng, L. 2017 Strouhal–Reynolds number relationship for flow past a circular cylinder. *J. Fluid Mech.* **832**, 170–188.

Jiang, H. & Cheng, L. 2018 Hydrodynamic characteristics of flow past a square cylinder at moderate Reynolds numbers. *Phys. Fluids* **30**, 104107.

Jiang, H. & Cheng, L. 2019 Transition to the secondary vortex street in the wake of a circular cylinder. *J. Fluid Mech.* **867**, 691–722.

Jiang, H., Cheng, L. & An, H. 2017*a* On numerical aspects of simulating flow past a circular cylinder. *Intl J. Numer. Meth. Fluids* **85**, 113–132.

JIANG, H., CHENG, L. & AN, H. 2018*a* Three-dimensional wake transition of a square cylinder. *J. Fluid Mech.* **842**, 102–127.

JIANG, H., CHENG, L., AN, H., TONG, F. & YANG, F. 2018*b*. Flow past a diamond cylinder at moderate Reynolds numbers. In *21st Australasian Fluid Mechanics Conference, Adelaide, Australia*.

JIANG, H., CHENG, L., DRAPER, S. & AN, H. 2017*b* Prediction of the secondary wake instability of a circular cylinder with direct numerical simulation. *Comput. Fluids* **149**, 172–180.

JIANG, H., CHENG, L., DRAPER, S., AN, H. & TONG, F. 2016 Three-dimensional direct numerical simulation of wake transitions of a circular cylinder. *J. Fluid Mech.* **801**, 353–391.

KARNIADAKIS, G.E. & SHERWIN, S.J. 2005 *Spectral/hp Element Methods for CFD*. Oxford University Press.

LEWEKE, T. & WILLIAMSON, C.H.K. 1998 Three-dimensional instabilities in wake transition. *Eur. J. Mech. (B/Fluids)* **17**, 571–586.

NG, Z.Y., VO, T., HUSSAM, W.K. & SHEARD, G.J. 2016 Two-dimensional wake dynamics behind cylinders with triangular cross-section under incidence angle variation. *J. Fluids Struct.* **63**, 302–324.

PARK, D. & YANG, K. 2016 Flow instabilities in the wake of a rounded square cylinder. *J. Fluid Mech.* **793**, 915–932.

POSDZIECH, O. & GRUNDMANN, R. 2001 Numerical simulation of the flow around an infinitely long circular cylinder in the transition regime. *Theor. Comput. Fluid Dyn.* **15**, 121–141.

ROBICHAUX, J., BALACHANDAR, S. & VANKA, S.P. 1999 Three-dimensional Floquet instability of the wake of square cylinder. *Phys. Fluids* **11**, 560–578.

SAHA, A.K. 2007 Far-wake characteristics of two-dimensional flow past a normal flat plate. *Phys. Fluids* **19**, 128110.

SERSON, D., MENEGHINI, J.R., CARMO, B.S., VOLPE, E.V. & GIORIA, R.S. 2014 Wake transition in the flow around a circular cylinder with a splitter plate. *J. Fluid Mech.* **755**, 582–602.

SHEARD, G.J., FITZGERALD, M.J. & RYAN, K. 2009 Cylinders with square cross-section: wake instabilities with incidence angle variation. *J. Fluid Mech.* **630**, 43–69.

SHEARD, G.J., THOMPSON, M.C. & HOURIGAN, K. 2003 A coupled Landau model describing the Strouhal–Reynolds number profile of a three-dimensional circular cylinder wake. *Phys. Fluids* **15**, L68–L71.

SOHANKAR, A., NORBERG, C. & DAVIDSON, L. 1999 Simulation of three-dimensional flow around a square cylinder at moderate Reynolds numbers. *Phys. Fluids* **11**, 288–306.

THOMPSON, M.C., LEWEKE, T. & WILLIAMSON, C.H.K. 2001 The physical mechanism of transition in bluff body wakes. *J. Fluids Struct.* **15**, 607–616.

THOMPSON, M.C., RADI, A., RAO, A., SHERIDAN, J. & HOURIGAN, K. 2014 Low-Reynolds-number wakes of elliptical cylinders: from the circular cylinder to the normal flat plate. *J. Fluid Mech.* **751**, 570–600.

TONG, X.H., LUO, S.C. & KHOO, B.C. 2008 Transition phenomena in the wake of an inclined square cylinder. *J. Fluids Struct.* **24**, 994–1005.

WILLIAMSON, C.H.K. 1996 Three-dimensional wake transition. *J. Fluid Mech.* **328**, 345–407.

YILDIRIM, I., RINDT, C.C.M. & VAN STEENHOVEN, A.A. 2013 Energy contents and vortex dynamics in Mode-C transition of wired-cylinder wake. *Phys. Fluids* **25**, 054103.

YOON, D., YANG, K. & CHOI, C. 2010 Flow past a square cylinder with an angle of incidence. *Phys. Fluids* **22**, 043603.

YOON, D., YANG, K. & CHOI, C. 2012 Three-dimensional wake structures and aerodynamic coefficients for flow past an inclined square cylinder. *J. Wind Engng Ind. Aerodyn.* **101**, 34–42.